



**HAL**  
open science

## Substitution-induced internal strain and high disorder in weakly radiation damaged hydrothermal zircon from Mt. Malosa, Malawi

Ulf Kempe, Ghislain Trullenque, Rainer Thomas, Sergey Sergeev, Sergej Presnyakov, Nikolai Rodionov, Cameliu Himcinschi

► **To cite this version:**

Ulf Kempe, Ghislain Trullenque, Rainer Thomas, Sergey Sergeev, Sergej Presnyakov, et al.. Substitution-induced internal strain and high disorder in weakly radiation damaged hydrothermal zircon from Mt. Malosa, Malawi. *European Journal of Mineralogy*, 2018, 30, pp.659 - 679. 10.1127/ejm/2018/0030-2739 . hal-04166714

**HAL Id: hal-04166714**

**<https://hal.science/hal-04166714>**

Submitted on 20 Jul 2023

**HAL** is a multi-disciplinary open access archive for the deposit and dissemination of scientific research documents, whether they are published or not. The documents may come from teaching and research institutions in France or abroad, or from public or private research centers.

L'archive ouverte pluridisciplinaire **HAL**, est destinée au dépôt et à la diffusion de documents scientifiques de niveau recherche, publiés ou non, émanant des établissements d'enseignement et de recherche français ou étrangers, des laboratoires publics ou privés.

## Substitution-induced internal strain and high disorder in weakly radiation damaged hydrothermal zircon from Mt. Malosa, Malawi

ULF KEMPE<sup>1,\*</sup>, GHISLAIN TRULLENQUE<sup>2</sup>, RAINER THOMAS<sup>3</sup>, SERGEY SERGEEV<sup>4,6</sup>, SERGEJ PRESNYAKOV<sup>4</sup>, NIKOLAI RODIONOV<sup>4</sup> and CAMELIU HIMCINSCHI<sup>5</sup>

<sup>1</sup> Institut für Mineralogie, TU Bergakademie Freiberg, Brennhausgasse 14, 09596 Freiberg, Germany

\*Corresponding author, e-mail: [kempe@mineral.tu-freiberg.de](mailto:kempe@mineral.tu-freiberg.de)

<sup>2</sup> Oxford Instruments GmbH, Otto-von-Guericke-Ring10, 65205 Wiesbaden, Germany

<sup>3</sup> Deutsches GeoForschung Zentrum GFZ Potsdam, Telegrafenberg, 14473 Potsdam, Germany

<sup>4</sup> Centre of Isotopic Research, Karpinsky Russian Geological Research Institute (VSEGEI), Srednyi prospect 74, 199106 St. Petersburg, Russia

<sup>5</sup> TU Bergakademie Freiberg, Institut für Theoretische Physik, Leipziger Straße 23, 09596 Freiberg, Germany

<sup>6</sup> Institute of Earth Sciences, St. Petersburg State University, Universitetskaya nab. 7/9, 199034 St. Petersburg, Russia

**Abstract:** Characteristics of two types of zircon from a single rock sample from the Mt. Malosa Massif, Malawi, are presented. According to Raman spectroscopy, the structure of a yellow hydrothermal zircon grown within a miarolitic cavity seems to be highly disordered. However, the extent of radiation damage calculated from the Raman data exceeds the degree of disorder that can be ascribed to the maximum possible internal radiation dose received by the crystals since their formation. Optical birefringence suggests an ordering degree close to that of well-ordered zircon for most areas in the crystals as may be also concluded from the always sharp electron backscattered diffraction (EBSD) patterns. Brownish zircon crystals from the wall-rock of the cavity of the same sample are most probably magmatic in origin. These crystals display a high degree of order and common low contents of radioactive and other substituting elements (<0.5 wt% in total). The absolute ages and U and Th contents of both zircon types were verified by U–Pb sensitive high-resolution ion microprobe (SHRIMP) analysis and the magmatic zircon is found to be significantly older ( $292 \pm 10$  Ma) than the hydrothermal one ( $121 \pm 9$  Ma). The apparent discrepancies between the data obtained by various methods for the hydrothermal zircon may be explained taking into account the unusual chemical composition and structural particularities established as well as (re-)interpreting the physical meaning of the variations in band positions and band widths in the Raman spectra. Electron probe microanalysis (EPMA) shows relatively high contents of yttrium (up to 4.8 wt%  $Y_2O_3$ ) and the rare earth elements (REE, up to 1.5 wt% oxides in total), occasionally also of thorium (up to 0.8 wt%  $ThO_2$ ). The charge unbalance caused by the substitution of trivalent elements is not compensated by coupled substitution involving other elements like phosphorus, niobium or uranium. The unusual composition and substitution is reflected by the related cathodoluminescence (CL) spectra consisting of sharp and intense line emissions from  $Dy^{3+}$ ,  $Sm^{3+}$ ,  $Nd^{3+}$  and  $Tb^{3+}$  centers in zircon. The broad band emissions normally observed in well-ordered zircon are quenched. Orientation contrast imaging (OCI) and EBSD reveal textures consisting of relatively large strained orientation domains showing a distinct distribution pattern. We suggest that internal tensional strain induced by substitution, vacancy formation and related domain formation may explain the data. Possible consequences of these findings for the understanding of the formation of metamict zircon should be considered in future research.

**Key-words:** zircon; strain; EBSD; Raman; disorder; metamict; substitution.

### 1. Introduction

Due to the exceptional behavior and widespread occurrence of zircon, its U–Pb geochronology is of great importance for absolute age determination in geosciences (e.g., Davis *et al.*, 2003; Harley & Kelly, 2007). Another topic of long-lasting scientific interest is the use of zircon ceramics in the storage of radioactive waste (e.g., Gentry *et al.*, 1982; Ewing *et al.*, 1995; Ewing, 2001). Under both aspects, an understanding of the phenomenon of zircon

metamictization (occurrence of an isotropic state of secondary origin; Syme *et al.*, 1977) is crucial because metamict zircon may not retain the required original age information (e.g., Davis *et al.*, 2003; Kempe *et al.*, 2015) and is not always resistant to secondary alteration under hydrothermal conditions (e.g., Geisler *et al.*, 2003; Anderson *et al.*, 2008; Soman *et al.*, 2010; Wang *et al.*, 2014). It is now generally accepted that metamictization of natural zircon results from the accumulated  $\alpha$ -recoil damage occurring during radioactive decay of U and Th

incorporated in the zircon structure (*e.g.*, Ewing *et al.*, 2003).

Beginning from the pioneering work by Nasdala *et al.* (1995), a growing number of authors have made use of the Raman microprobe technique to evaluate the degree of metamictization of natural zircon on a local scale (see, *e.g.*, Nasdala *et al.*, 2003). Advantages of this method are the high spatial resolution down to micrometer-scale and the virtual absence of any sample damage at low laser powers. Additionally, there is no need in sophisticated sample preparation.

According to the modern concepts of zircon metamictization, the loss of long-range order (periodicity of the structure according to the lattice model) on nano- to micro-scale accompanied by a loss of short-range order (fixed arrangement of the nearest neighbors around single atoms/ions) results from the growth of structural domains strongly affected by  $\alpha$ -recoil damage and their transformation to a metamict (fully disordered) state (Murakami *et al.*, 1991; Ewing *et al.*, 2003). This concept implies that systematic changes in density (Holland & Gottfried, 1955; Özkan, 1976; Murakami *et al.*, 1991), hardness (Özkan, 1976; Chakoumakos *et al.*, 1991; Oliver *et al.*, 1994), birefringence (Holland & Gottfried, 1955; Sahama, 1981; Palenik *et al.*, 2003), and diffraction properties (Holland & Gottfried, 1955; Murakami *et al.*, 1991; Ríos *et al.*, 2000b; Nasdala *et al.*, 2002b) as well as in infrared (IR; Akhmatova & Leonova, 1961; Wasilewski *et al.*, 1973; Delines *et al.*, 1977; Woodhead *et al.*, 1991; Zhang & Salje, 2001), Raman (Nasdala *et al.*, 1995; Zhang *et al.*, 2000; Nasdala *et al.*, 2001; Nasdala *et al.*, 2002b, 2003, Marsellos & Garvers, 2010), electron paramagnetic resonance (EPR; Nasdala *et al.*, 2003; Kempe *et al.*, 2010) and luminescence characteristics (Lenz & Nasdala, 2015) are correlated with each other and with the dose accumulated.

A zircon sample from Mt. Malosa, Malawi, investigated here in more detail, demonstrates that this is not always the case. Some natural zircon may display a high degree of disorder by one method but does not show it at the same extent when investigated by other techniques. As will be discussed in more detail below, such findings may indicate that other processes leading to high disorder in natural zircon besides irradiation damage should be considered.

Earlier, this Malawi sample was included into a sample set investigated by several spectroscopic techniques including optical absorption (OA), electron paramagnetic resonance (EPR), Raman, and time-resolved photoluminescence (TRL) spectroscopy (Kempe *et al.*, 2010; Kempe *et al.*, 2016). According to the Raman data and using the classification proposed by Nasdala *et al.* (1995, 1998), the disorder in the Mt. Malosa zircon should be estimated as “intermediate to metamict” (Kempe *et al.*, 2010). However, subsequent evaluation of thin sections of this material in transmitted light suggests that the order in these crystals is rather well preserved with the possible exception of some high-Th growth zones. This finding prompted additional studies.

Several facts reported in recent publications or found during our own research question the assumption that the

theory of zircon metamictization has already reached maturity. In particular, it was mentioned that the formation of disordered areas in zircon is sometimes related to hydrothermal alteration rather than to radioactive decay (Zhirov, 1952; Rudenko, 1968; Kempe *et al.*, 2004). Anderson *et al.* (2008) reported trace element-poor, nearly U- and Th-free zircon material in late cracks within altered, trace element-rich metamict zircon from Nova Scotia. The former areas were nearly amorphous according to the absence of TEM electron diffraction patterns while the latter showed a somewhat higher ordering degree.

Kempe *et al.* (2010) found a green natural zircon where the significant shift in the position of the Raman bands was not accompanied by related band broadening. Furthermore, an extremely U-rich, green zircon from Sri Lanka was found to be rather well-ordered (Kempe *et al.*, 2016). We also reported an apparently well-ordered, extremely U-rich zircon from Muruntau (Kempe *et al.*, 2015).

In the following text, we will restrict our self to the case of the Malawi zircon under consideration here. Additional work is needed to clarify the situation in all cases mentioned and to understand their relations to the general phenomenon of zircon metamictization.

## 2. Materials and methods

### 2.1. Geological background

The sample studied comes from a miarolitic cavity as typically observed in the roof zone of the alkaline granite massif at the Mt. Malosa, Zomba plateau, Chilwa alkaline province, southern Malawi (*e.g.*, Eby *et al.*, 1995; Högdahl & Jonsson, 1999; Soman *et al.*, 2010). The Chilwa alkaline province is located at the southern extension of the East African rift system (Woolley & Platt, 1986; Woolley & Jones, 1987; Eby *et al.*, 1995). The intrusive rocks vary in composition from nepheline syenite and quartz syenite to granite and include also carbonatites (Platt & Woolley, 1986; Woolley & Platt, 1986; Woolley & Jones, 1987; Eby *et al.*, 1995). Obviously, the formation of the complex is related to rifting in this part of the continent (Woolley, 1987). At surface, the Zomba-Malosa complex forms a pear-shaped body in the northern part of the province. The central part is formed by syenite surrounded by rings of quartz-syenite and granite (Woolley & Jones, 1987; Eby *et al.*, 1995). The area around Mt. Malosa exhibits many pegmatite cavities carrying exotic Th-rich Zr–Nb–REE–Be mineralization (Högdahl & Jonsson, 1999, Guastoni & Pezzotta, 2007; Guastoni *et al.*, 2009). Several stages of hydrothermal activity close to each other in formation time were observed according to replacement relations within the pegmatites (Guastoni *et al.*, 2009; Soman *et al.*, 2010). Similar mineralization is also present elsewhere in the area (Platt *et al.*, 1987).

Three types of zircon may be distinguished in the pegmatites according to Högdahl & Jonsson (1999): (1) translucent reddish-brownish crystals with a complex of simple forms, (2) opaque short prismatic brownish zircon and (3) translucent prismatic yellow crystals. The zircon

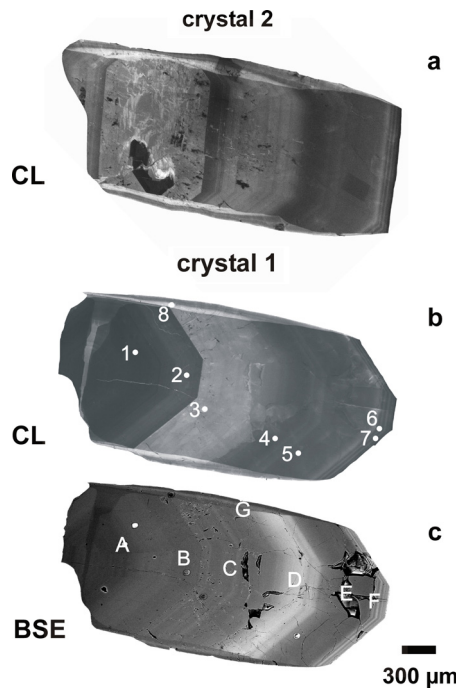


Fig. 1. Cathodoluminescence (CL) and BSE images of the two Type 1 yellowish crystals used for EMPA, CL spectroscopy, SHRIMP and Raman spectroscopy (crystal 1) and oriented-contrast (OC) imaging, EBSD and Raman spectroscopy (crystal 2), respectively. The numbers and locations of the spots in Fig. 1b correspond to the numbers of analyses obtained by EMPA, CL spectroscopy, SHRIMP and Raman spectroscopy in other figures, tables and in the text. SHRIMP spots are visible in the BSE image taken after SHRIMP analysis.

investigated in this work belongs to the first and third types. Earlier, Soman *et al.* (2010) have investigated a brownish, opaque zircon crystal of the second type displaying significant secondary alteration features.

## 2.2. Sample and sample preparation

The crystals of yellowish translucent hydrothermal zircon used in the present study were prepared from a single rock sample from the wall of a miarolitic cavity in the alkaline granite. Crystals formed in free space together with some quartz and riebeckite. The growth proceeded from the wall to the center of the cavity. All crystals exhibit simple combinations of the  $\{100\}$  prism and the  $\{101\}$  dipyrmaid and do not show any signs of deformation. We conclude that the zircon crystals experienced only fluid pressure and that only fluid-induced brittle but no plastic deformation could have occurred. As mentioned above, the degree of disorder in a yellow transparent crystal termination used in our previous work is intermediate to metamict according to Raman spectroscopy (*cf.* classification by Nasdala *et al.*, 1995, 1998) with an average full-width at half maximum (FWHM) of  $18.3 \pm 1.0 \text{ cm}^{-1}$  for the  $\nu_3$  ( $B_{1g}$ ) mode of the  $[\text{SiO}_4]$  tetrahedral groups (Kempe *et al.*, 2010). Subsequent measurements on several other crystals yielded very similar results.

Examination of several dozens of grains under a binocular microscope showed that there is a common growth zoning which can be paralleled to the internal texture revealed in five crystals investigated in polished sections by scanning electron microscopy with back-scattered electron (BSE) and cathodoluminescence (CL) imaging irrespective of the variable crystal sizes (Fig. 1): (1) A core of yellow to greenish coloration with variable internal textures including sector zoning (zone A in Fig. 1c) is surrounded by an outer zone not clearly distinguishable under the optical microscope but clearly visible in CL and BSE images (zone B in Fig. 1c). (2) The next zone C is cloudy with many cracks and voids and displays yellowish-brownish coloration and normal growth zoning under BSE and CL. (3) The transparent yellow upper crystal termination consists of zone D exceptionally bright in the backscattered electron (BSE) contrast with normal growth zoning followed by the nearly homogeneous zone E darker in BSE and, finally, the thin zone F with distinct oscillatory growth zoning at the rim. Sector zoning is well expressed by thin sector G at the  $\{100\}$  prism faces in BSE and CL images (Fig. 1c). In few crystals grown sub-parallel to the wall of the cavity, the same zoning may be also followed in the opposite direction from the crystal core.

One crystal of this hydrothermal zircon was oriented parallel to the *c* axis using a spindle stage and mounted into a polished thin section for optical microscopy. Two other crystals from the same sample were selected for detailed local analysis. One of these crystals was mounted together with other zircon in a polished section and gold coated for BSE and CL imaging and subsequent SHRIMP analysis. Following this procedure, the gold was removed and the section investigated by Raman spectroscopy. Prior to the following electron probe microanalysis and CL spectroscopy, the sample was carbon coated to prevent build-up of electrical charge.

The second crystal was polished with silica gel for orientation contrast (OC) and CL imaging, electron-backscattered diffraction (EBSD), and Raman spectroscopy. The sample was coated with a 2 nm thick platinum film. This film was later removed to allow subsequent Raman measurements.

The coarse-grained host rock of the sample around the cavity contained the second zircon type – brownish crystals of short-prismatic habit with a combination of a dominant  $\{110\}$  prism (occasionally also with a weakly developed  $\{100\}$  prism) and a  $\{101\}$  dipyrmaid. These crystals display normal growth zoning, sector zoning and some recrystallisation features visible under the microscope and in BSE and CL images (Fig. 2). The mode of occurrence of this zircon type forming intergrowth with rock-forming minerals suggests a magmatic origin. To verify the genetic relationships between the two zircon types, two crystals of the brownish zircon were also analyzed. One was mounted together with one yellowish crystal of hydrothermal zircon in a polished section for the investigation procedure including BSE and CL imaging, U-Pb SHRIMP analysis, Raman spectroscopy, EMPA and

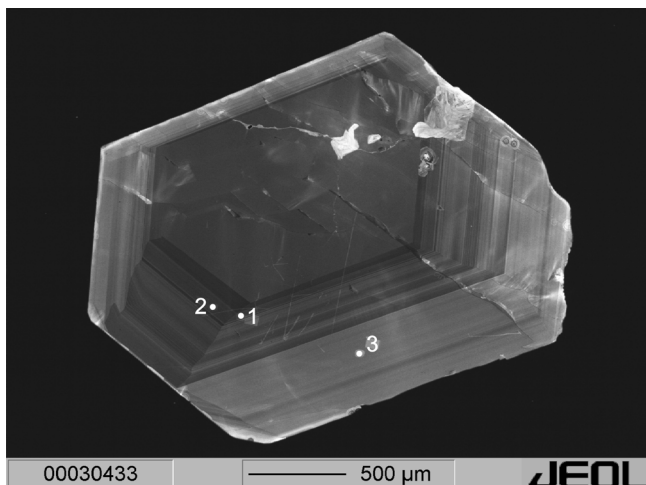


Fig. 2. CL image of the brownish Type 2 crystal of magmatic zircon from the host rock used for EMPA, CL spectroscopy, SHRIMP and Raman spectroscopy. The location numbers of the spots in the figure correspond to numbers of EMPA, CL, SHRIMP and Raman analyses in the figures, tables and in the text.

CL spectroscopy. The other brownish crystal was used for a thin section for optical microscopy with orientation of the *c* axis parallel to the sample surface.

### 2.3. Methods

Optical properties in transmitted light were investigated using a Carl Zeiss Axioskop 40. The birefringence was calculated from the interference colors as described by Palenik *et al.* (2003) except that the thickness of crystal section in the point of measurement of the thin section was determined using the micrometer drive of the microscope calibrated to a set of polished diamond slabs with known thicknesses determined by a micrometer. The estimated error in birefringence is about  $\pm 0.002$ , somewhat higher than in the work by Palenik *et al.* (2003).

For electron microscopy, a Jeol JSM 6400 equipped with a Tracor/Noran Series II energy dispersive X-ray detection system, an Oxford Mini-CL detector for CL imaging and a Mono-CL 1 mirror system combined with a transportable spectrograph for CL spectroscopy (Götze & Kempe, 2008) was used. For CL and BSE imaging, the SEM was operated at 20 kV and 0.6 nA; CL spectra were taken subsequent to SHRIMP measurements with a defocused electron beam (diameter about 20  $\mu\text{m}$  adjusted to the diameter of adjacent spots from SHRIMP measurements) at 20 kV and 3.56 nA. Calibration was done using mercury and argon emission lines for the blue and red part of the spectrum, respectively. The acquisition time for the spectra was 100 s. Due to the low signal intensities, no CL spectra could be obtained with a focused beam from a particular Th-rich growth zone appearing bright in the BSE images of the crystal where no larger areas without cracks or voids could be found (cf. below). To display orientation contrast (OC), BSE imaging was performed at 3 kV and 3.4 nA with a working distance of 8 mm. Additional OC images were obtained using a cold field

emission JSM 7500F at the Jeol Demonstration Center in Garching near Munich (Germany). A large-angle BSE (LAGE) detector operated at 1 kV and 50 pA at a working distance of 4 mm yielded an increased stereographic contrast.

Four EBSD maps were acquired using a Nordlys S camera mounted on a ZEISS SUPRA 55VP operated in the high vacuum mode at 20 kV, 1.5 nA probe current and 13 mm WD with step sizes of 200 nm in variable grids. The sample tilt was 70°. The Channel 5 (Oxford Instruments) software was used for data acquisition and evaluation.

For SHRIMP measurements, the two chosen crystals – one yellow of the first type from the cavity and one brownish of the second type from the wall rock – were mounted in epoxy resin together with reference zircon TEMORA 1 (Middledale Gabbroic Diorite, New South Wales, Australia; Black *et al.*, 2003) and reference zircon 91500 (Wiedenbeck *et al.*, 1995), polished and gold coated. Before SHRIMP analysis, the grains were documented by reflected and transmitted light photographs as well as CL and BSE imaging. SHRIMP measurements were carried out at the Centre of Isotopic Research of the Karpinsky All-Russian Geological Research Institute (VSEGEI), St. Petersburg, Russia using SHRIMP II. The spot size was set at 20  $\mu\text{m}$  and the beam current at 4 nA. Five mass scans were collected for each analysis. Mass resolution at the mass 254UO was 5200 at 1% peak height. Data reduction was performed using the procedure proposed by Williams (1998) applying the SQUID Excel Macro by Ludwig (2000). The Pb/U ratios were normalized relative to a  $^{206}\text{Pb}/^{238}\text{U}$  value of 0.0668 for the TEMORA 1 reference equivalent to an age of 416.75 Ma (Black *et al.*, 2003). Reference zircon 91500 was used as concentration reference material (81.2 ppm U). Measured against the TEMORA 1 reference during the same session, it showed some enhanced isotope data scatter with a calculated Concordia age of  $1062 \pm 27$  Ma ( $n = 5$ ; accepted value  $1065.4 \pm 0.4$  Ma).

Subsequent Raman, EMPA and CL measurements were made as close as possible adjacent to the SHRIMP spots with locations carefully chosen within the same growth zones defined by optical, BSE and CL imaging. Additional locations were also checked, especially when fine zoning or voids and cracks in the crystal avoided SHRIMP measurements at a 20  $\mu\text{m}$  scale (as in the Th-rich growth zone mentioned above and at the crystal rim). Some Raman measurements were also made within the SHRIMP spots but yielded essentially identical results as in the adjacent areas (cf. Nasdala *et al.*, 1998).

Microprobe analysis was performed with an SX-100 microprobe (CAMECA) applying the standard method used at the GeoForschungsZentrum, Potsdam (e.g., Anderson *et al.*, 2008). The acceleration voltage was 20 kV and the beam current 40 nA. Natural and synthetic zircon (Zr, Si), HfO<sub>2</sub> (Hf), Y and rare earth element (REE) phosphates (REE, Y, Sc, and P), pure metals (Ti, Nb, U, Th), hematite (Fe), corundum (Al), wollastonite (Ca), and vanadinite (Pb) were used as references. Counting times were 20 s for Si *K* $\alpha$ , Zr *L* $\alpha$ , Ca *K* $\alpha$ , and Al *K* $\alpha$ ; 30 s for Fe

$K\alpha$ ,  $Y L\alpha$ ,  $Sc K\alpha$ , and  $P K\alpha$  and 50 s for the other elements (Hf  $L\beta$ , Ce  $L\alpha$ , Nd  $L\beta$ , Sm  $L\beta$ , Gd  $L\beta$ , Dy  $L\beta$ , Yb  $L\alpha$ , Ti  $K\alpha$ , Nb  $L\alpha$ , Th  $M\alpha$ , U  $M\beta$ , and Pb  $M\beta$ ) both on the peak and on the carefully chosen background positions on both sides of the peaks. Iron, Hf, Ce, Nd, Sm, Gd, Dy and Yb were measured on a LiF crystal while P, Ca, Sc, Ti, Th, U, and Pb were measured on PET and Si, Zr, Nb, Al and Y on a TAP crystal. The limits of detection were: Hf – 1900 ppm, Fe – 400 ppm, Al – 130 ppm, Ca – 180 ppm, Sc – 160 ppm, Nb – 200 ppm, Th – 640 ppm, U – 840 ppm, Pb – 1100 ppm, Y – 440 ppm, Ce – 630 ppm, Nd – 710 ppm, Sm – 720 ppm, Gd – 590 ppm, Dy – 600 ppm and Yb – 600 ppm. Phosphorus was not found in any analysis; the somewhat overestimated theoretical detection limit for this element was at about 340 ppm. A search for F was also not successful. Because of the rather high EMPA detection limits for Th, U and Pb, mainly results from SHRIMP measurements for these elements will be used in the following discussion.

Raman measurements were done with a Jobin Yvon LABRAM HR800 operated in the confocal mode (pinhole 100  $\mu\text{m}$ ) at room temperature using the 488 nm line of a Innova 70C Coherent Ar<sup>+</sup> laser (laser power 14 mW on the sample). The laser was focused on the sample surface using an Olympus microscope with a 100 $\times$  objective. The spectral resolution of the system was 0.6  $\text{cm}^{-1}$ .

#### 2.4. Comparison of spatial resolution of Raman spectroscopy and EBSD

Because we will compare long-range order probed by EBSD with the short-range order checked by Raman spectroscopy, it is useful to recall and discuss here to some extent the spatial resolution of the two methods.

Raman spectroscopy probes a significantly larger volume compared to EBSD. In modern Raman microprobes, the focused beam may approach about 1  $\mu\text{m}$  as a minimum diameter constraining the lateral resolution of the method (Bruneel *et al.*, 2002; Nasdala *et al.*, 2005). A cone of the laser light is penetrating further into the sample without sharp depth restrictions for samples transparent in the region of the laser wavelength used as in the present case for zircon. Depth resolution may be increased applying confocal optics (Puppels *et al.*, 1991; Nasdala *et al.*, 1998; Bruneel *et al.*, 2002; Nasdala *et al.*, 2003). It is sometimes believed that depth resolution may even reach 2  $\mu\text{m}$  for crystalline materials (Nasdala *et al.*, 2003, 2005). However, closer evaluation shows that this is by far a too optimistic value. Normally, about 7  $\mu\text{m}$  or more may be expected for transparent crystalline materials (Bruneel *et al.*, 2002; Kranert *et al.*, 2016). As outlined by Everall (2000), this is mainly due to the refraction at the air – sample interface when dry objectives are used. Clearly, this effect is pronounced for zircon with its high refraction indices (1.92–2.02 for crystalline and 1.75 for metamict material). We have further verified the sampling depth for our instrumental setup by a simple experiment using one and the same crystal of fluorite and zircon, respectively, to prepare a thin section (30  $\mu\text{m}$  thickness)

from one half of the sample and a thick section (about 1 mm thickness for zircon and about 3 mm for fluorite limited by the sample sizes) from the other. The sample pairs were measured in the confocal mode (pinhole 100  $\mu\text{m}$ ) on a T64000 (fluorite) and a Jobin Yvon LABRAM HR800 (zircon) in one session under the same conditions with the beam focused on the polished surface. In both cases, the Raman signal of the fluorite and zircon modes increased by about 50% in intensity when going from the thin to the thick section indicating detection of some additional Raman scattering from sample areas even below 30  $\mu\text{m}$ . Recently, Presser & Glotzbach (2009) reached very similar conclusions on local resolution and sampling depth for zircon and other transparent materials.

Compared to Raman spectroscopy, spatial resolution of EBSD mapping is exceptionally high. The EBSD signal derives entirely from a near-surface zone only some nm thick. Therefore, spatial resolution depends mostly on the electron probe diameter, acceleration voltage, and the average atomic number of the sample and is clearly below 40 nm in the given case, considering the relatively high average atomic number of zircon with  $Z > 14$  (*cf.* Humphreys, 2001; Dingley, 2004).

### 3. Results

#### 3.1. Polarized-light microscopy, optical absorption and cathodoluminescence spectra

The birefringence in yellowish Type 1 zircon is nearly constant over the whole grain (red, sometimes yellowish of second order for sample thicknesses of about 20  $\mu\text{m}$ ), mostly approaching 0.050 (0.048–0.050) indicative of well-ordered zircon. At the yellow transparent crystal termination, there is a zone with a distinct decrease in birefringence down to 0.031 (0.044–0.031). This zone coincides with the mentioned Th-rich zone D appearing bright in BSE images (Fig. 1). Palenik *et al.* (2003) found a linear correlation between birefringence and radiation dose for Sri Lanka zircons. This, in principle, opens the opportunity to estimate received radiation doses from birefringence measurements for samples from this location. It is, of course, dangerous to apply this relationship to other zircons with a different thermal history. Provided that our crystals and Sri Lanka zircons have not experienced significant re-heating after formation and that the indicated disorder is related to radiation damage only, an estimate of the received radiation dose may be attempted basing on the measured birefringence. For the zone under discussion, birefringence would correspond to a received radiation dose of  $3.7 \times 10^{18}$   $\alpha$ -events/g. Note, however, that at least Sri Lanka zircon experienced some kind of secondary annealing (Palenik *et al.*, 2003; Nasdala *et al.*, 2004). Therefore, such an estimate is certainly in error and can only be seen as a very rough approximation. At the crystal rim F, birefringence decreases down to 0.038 (0.046–0.038) in some of the fine, Th-rich oscillatory growth zones which would correspond to an estimated dose of  $2.2 \times 10^{18}$   $\alpha$ -events/g, respectively.

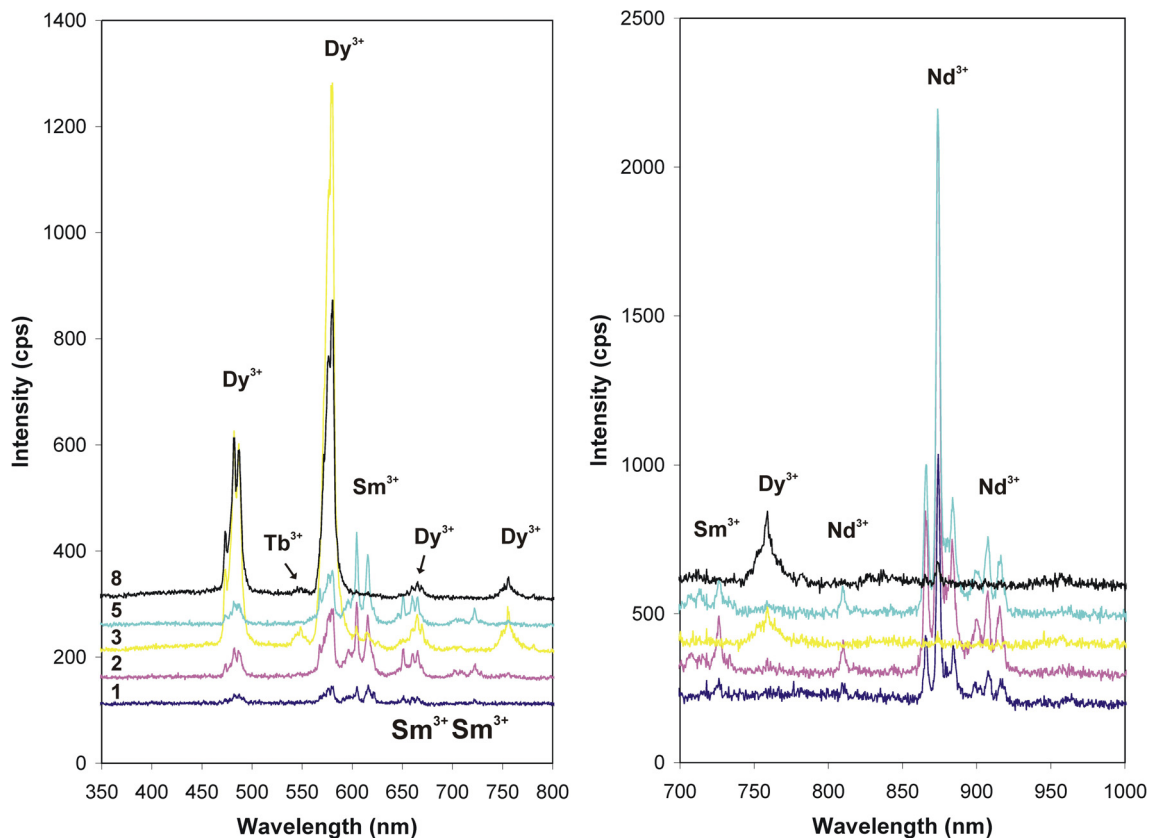


Fig. 3. CL spectra of Type 1 REE-rich yellowish hydrothermal zircon (crystal 1) from the cavity. Spot numbers correspond to those in Fig. 1b.

In the brownish Type 2 zircon from the wall rock, the birefringence is nearly constant around 0.054 indicating well-ordered zircon (Holland & Gottfried, 1955; Sahama, 1981). Note that the maximum birefringence suggested by the model proposed by Palenik *et al.* (2003) is 0.0486 at zero dose, somewhat below the expected value of 0.055.

According to optical absorption spectroscopy (Kempe *et al.*, 2010, 2016), the yellow color of the zircon crystals from the cavity is caused by an edge-like absorption appearing at about 450 nm. Probably, this absorption is related to charge transfer transitions involving REE that may have variable valance states in zircon as Ce, Pr, Eu and/or Tb. Another possible explanation is a “shift” of the absorption edge into the visible range due to lattice defects accumulated from radioactive irradiation (Kempe *et al.*, 2016). The sharp absorption lines appearing in the red part of the spectra are related to  $\text{Nd}^{3+}$  and  $\text{Er}^{3+}$ , but they have only negligible influence on the visible color. Remarkably, absorption lines from  $\text{U}^{4+}$  were not observed in the spectra (Kempe *et al.*, 2016).

Cathodoluminescence spectroscopy revealed that the light emitted from yellowish Type 1 zircon is, if detectable, exclusively related to sharp line emissions from  $\text{REE}^{3+}$  centers (Fig. 3). Identification of the emission lines was achieved using published luminescence spectra of synthetic zircon intentionally doped with single rare earth elements and considering the observed intensity relations and fine structures in these spectra besides line positions. Except general intensity variations, two principal types of

spectra can be distinguished in the yellow zircon: (1) CL spectra of the yellowish-green core region (central part and rim; zones A and B) and of the yellow crystal area E between the zone D with quenched luminescence on one side and the oscillatory growth zoning at the upper crystal rim F on the other are of the first type (spectra 1, 2 and 5 in Fig. 3). (2) The yellowish-brown intermediate region C between the core (A+B) and the zone D with quenched CL as well as the growth sectors G of the  $\{100\}$  prism exhibit the second type (spectra 3 and 8 in Fig. 3).

For the second-type spectra, CL emission is dominated by four transitions occurring in  $\text{Dy}^{3+}$ , namely  ${}^4\text{F}_{9/2} \rightarrow {}^6\text{H}_{15/2}$  centered at about 480 nm,  ${}^4\text{F}_{9/2} \rightarrow {}^6\text{H}_{13/2}$  (575 nm),  ${}^4\text{F}_{9/2} \rightarrow {}^6\text{H}_{11/2}$  (665 nm) and  ${}^4\text{F}_{9/2} \rightarrow {}^6\text{H}_{9/2}$  (755 nm). Similar spectra for  $\text{Dy}^{3+}$  were reported by Votyakov & Samojlov (1981), Cesbron *et al.* (1995), Karali *et al.* (2000), Friis *et al.* (2010) and – for a part of the related spectral range – by Trofimov (1962), Gaft *et al.* (2000), Finch *et al.* (2004), Nasdala *et al.* (2003) and Lenz & Nasdala (2015). Our spectra are most similar to the spectrum published by Friis *et al.* (2010) obtained by photoluminescence spectroscopy, especially considering intensity relations and the resolved fine structure of the lines. Besides the intense emissions from  $\text{Dy}^{3+}$ , there are only weak lines from  $\text{Sm}^{3+}$  in these spectra at 610 nm (*cf.* below) and an additional line at 545 nm (Fig. 3). The latter signal may be interpreted to arise from  $\text{Tb}^{3+}$  or  $\text{Er}^{3+}$ . Spectra of  $\text{Er}^{3+}$  were published by Votyakov *et al.* (1985, X-ray luminescence), Cesbron *et al.* (1995, CL),

Karali *et al.* (2000, radio- and thermoluminescence), Gaft *et al.* (2000, time-resolved photoluminescence) and partly by Nasdala *et al.* (2003, photoluminescence), spectra for  $Tb^{3+}$  in Iacconi & Caruba (1980, thermoluminescence), Votyakov & Samojlov (1981, thermoluminescence), Votyakov *et al.* (1985), Iacconi (1995), Cesbron *et al.* (1995), Gaft *et al.* (2000) and, for a part of the relevant spectral range, in Trofimov (1962, photoluminescence). Considering published data, we assign the emission under question to the  $^5D_4 \rightarrow ^7F_5$  transition in  $Tb^{3+}$  because: (1) the emission in  $Er^{3+}$  in this range is centered at somewhat higher wavelengths (about 550–555 nm); (2) the related emission in  $Tb^{3+}$  is by far the most intense in X-ray luminescence and thermoluminescence (normally exhibiting similar intensity relations and fine structures as in CL) while this is not the case for  $Er^{3+}$ .

The CL spectra of the first type differ significantly from the second type described above. In the first type of spectra, there is a strong decrease in the relative emission intensities of the  $Dy^{3+}$  lines and an increase in the intensity of the emission lines from  $Sm^{3+}$ . The latter show the typical intensity relations and fine structure transitions of the type  $^4G_{5/2} \rightarrow ^6H_{7/2}$  centered at 605 nm,  $^4G_{5/2} \rightarrow ^6H_{9/2}$  (660 nm), and  $^4G_{5/2} \rightarrow ^6H_{11/2}$  (703–728 nm). Fine structure lines from the  $^4G_{5/2} \rightarrow ^6H_{5/2}$  transition also occur but overlap with the Dy emission at 580 nm. Similar spectra were reported by Cesbron *et al.* (1995), Gaft *et al.* (2000), Karali *et al.* (2000), Nasdala *et al.* (2003), Friis *et al.* (2010) and Lenz & Nasdala (2015) and – for a part of the range – by Trofimov (1962). Our spectra of  $Sm^{3+}$  show a close similarity to the spectra reported by Nasdala *et al.* (2003), Friis *et al.* (2010) and Lenz & Nasdala (2015).

Dramatic changes occur in the red part of the first-type CL spectra where strong lines appear at 810.0, 865.9, 873.7 (strongest), 879.0 (weak), 883.4, 889.4, 907.2 and 915.6 nm. We assign these emissions to the  $^4F_{5/2} \rightarrow ^4I_{9/2}$  (810 nm) and  $^4F_{3/2} \rightarrow ^4I_{9/2}$  (865–916 nm) transitions in  $Nd^{3+}$ . Luminescence spectra of  $Nd^{3+}$  in natural zircon are rarely reported in the literature because the Nd content in the mineral is normally low to very low. The photoluminescence spectra published by Nasdala *et al.* (2003) and Lenz *et al.* (2013) are similar in the fine structure and line positions but the one by the first authors differs strongly in intensity relations from the spectrum published by Lenz *et al.* (2013) and the spectra obtained in the present work.

The CL signal obtained for the brownish Type 2 zircon from the wall rock differs from that of the yellow zircon (Fig. 4). It is dominated by broad bands with only weak signals from REE<sup>3+</sup> centers, in particular from  $Dy^{3+}$  and  $Er^{3+}$ . Remarkably, only the  $^4F_{3/2} \rightarrow ^4I_{9/2}$  (404 nm) and  $^4F_{3/2} \rightarrow ^4I_{9/2}$  (471 nm) transitions in  $Er^{3+}$  are of notable intensity, while the transitions from lower lying levels, especially at 530 and 558 nm, are very weak. The most intense broad band luminescence appears in the yellow spectral range (centered at 580 nm) while the short-living “blue” band at about 420 nm is suppressed in intensity. Such a CL behavior is typical of well-ordered zircon with low REE contents (Kempe *et al.*, 2000).

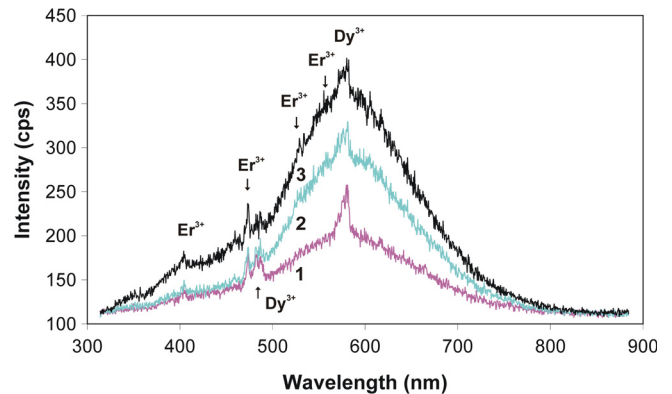


Fig. 4. CL spectra of Type 2 brownish magmatic zircon from the host rock. Spot numbers correspond to those in Fig. 2.

### 3.2. Chemical composition

The EMPA, EDX analysis in the SEM and the SHRIMP study revealed an unusual chemical composition for the yellow zircon from the cavity, but a common one for brownish zircon from the wall rock. Representative results of EMPA are listed in Table 1, the positions of related analytical spots is indicated in Fig. 1b and 2. Most remarkable are the very high contents of Y and the REE, occasionally including the light REE, in the yellow zircon. The Y contents are so high that they appear in the formula (0.01 atom per formula unit or more; Table 1).

The Th content is comparable to that of U in some areas, but may be significantly higher, reaching several thousands of ppm as in the broad zone D optically indistinguishable inside the yellow transparent crystal termination mentioned above. This zone D is clearly visible in the SEM because it appears bright in BSE images. In this Th-rich zone, Th is easily detected even by EDX. On the other hand, Fe, Ca and Al contents are always rather low to very low except some zones in the crystal core A. The Hf concentration around 1.5 wt% HfO<sub>2</sub> may be considered as typical of zircon in granitic rocks but is, in fact, a little enhanced compared to normal magmatic zircon from alkaline granites.

Although we have analyzed by EMPA only the even REE, pronounced fractionation of the REE is observed throughout the crystal as demonstrated by chondrite-normalized distribution patterns in Fig. 5. In the figure, Y is plotted instead of Ho; the absence of anomaly demonstrates that there was no significant Y/Ho fractionation (*cf.* Bau, 1996) during fluid evolution. The first REE distribution type (Fig. 5) is restricted to the core A. The distribution is concave with enrichment of the light (Ce) and heavy (Yb) REE and a relative depletion of the middle REE. The second type is observed for the zone B surrounding the core, the zone E in the outer yellow transparent crystal termination adjacent to the Th-rich zone and for a related narrow zone in the {100} growth sector G. Here, all REE including the light, middle and heavy groups are enriched although there is some relative depletion of Ce and some enrichment of Yb (Fig. 5). In all

Table 1. Selected EPMA data and relevant formulae for Type 1 yellowish hydrothermal zircon and Type 2 brownish magmatic zircon from Mt. Malosa (Malawi). Spot numbers are those shown in Figs. 1b and 2, respectively.

Point	Hydrothermal Type 1								Magmatic Type 2	
	1	2	3	4	5	6	7	8	1	2
SiO <sub>2</sub>	31.98	31.97	31.60	31.87	32.05	31.76	31.86	31.62	32.38	32.26
ZrO <sub>2</sub>	63.11	61.99	58.77	59.52	62.23	60.41	60.23	59.50	65.91	65.99
HfO <sub>2</sub>	1.49	1.41	1.45	1.46	1.62	1.41	1.36	1.36	0.99	1.19
Y <sub>2</sub> O <sub>3</sub>	0.33	1.79	4.76	3.29	1.19	2.79	3.07	4.24	<0.05	<0.05
Ce <sub>2</sub> O <sub>3</sub>	0.45	0.60	0.16	0.17	0.46	0.13	0.07	0.07	<0.07	<0.07
Nd <sub>2</sub> O <sub>3</sub>	0.08	0.38	0.04	0.04	0.57	0.04	0.06	<0.04	<0.04	<0.04
Sm <sub>2</sub> O <sub>3</sub>	<0.08	0.15	<0.08	0.08	0.18	<0.08	<0.08	<0.08	<0.08	<0.08
Gd <sub>2</sub> O <sub>3</sub>	0.06	0.17	0.28	0.43	0.26	0.39	0.30	0.33	<0.06	<0.06
Dy <sub>2</sub> O <sub>3</sub>	<0.05	0.14	0.44	0.52	0.19	0.37	0.32	0.41	<0.05	<0.05
Yb <sub>2</sub> O <sub>3</sub>	0.07	0.15	0.44	0.24	0.13	0.25	0.33	0.59	0.05	<0.05
UO <sub>2</sub>	<0.08	<0.08	<0.08	0.10	<0.08	<0.08	<0.08	<0.08	<0.08	<0.08
ThO <sub>2</sub>	<0.05	<0.05	0.09	0.75	0.11	0.49	0.43	<0.05	<0.05	<0.05
Nb <sub>2</sub> O <sub>5</sub>	0.28	0.24	0.13	0.23	0.23	0.17	0.13	0.03	0.02	0.02
TiO <sub>2</sub>	0.07	0.02	0.02	0.01	0.01	0.01	0.01	<0.01	<0.01	<0.01
Total	98.20*	99.01	98.18	98.71	99.23	98.15	98.22	98.17	99.35	99.46
Contents in wt%										
Formula units (apfu) calculated on a two-cation basis										
Zr	0.965	0.941	0.899	0.909	0.945	0.925	0.921	0.910	0.992	0.993
Hf	0.013	0.013	0.013	0.013	0.014	0.013	0.012	0.012	0.009	0.010
Y	0.006	0.030	0.079	0.055	0.020	0.047	0.051	0.071	<0.001	<0.001
Ce	0.005	0.007	0.002	0.002	0.005	0.002	0.001	0.001	<0.001	<0.001
Nd	0.001	0.004	0.001	<0.001	0.006	<0.001	0.001	<0.001	<0.001	<0.001
Sm	<0.001	0.002	<0.001	0.001	0.002	<0.001	<0.001	<0.001	<0.001	<0.001
Gd	0.001	0.002	0.003	0.005	0.003	0.004	0.003	0.003	<0.001	<0.001
Dy	<0.001	0.001	0.005	0.005	0.002	0.004	0.003	0.004	<0.001	<0.001
Yb	0.001	0.001	0.004	0.002	0.001	0.002	0.003	0.006	<0.001	<0.001
U	<0.001	<0.001	<0.001	0.001	<0.001	<0.001	<0.001	<0.001	<0.001	<0.001
Th	<0.001	<0.001	0.001	0.005	0.001	0.004	0.003	<0.001	<0.001	<0.001
Nb	0.004	0.003	0.002	0.003	0.003	0.002	0.002	<0.001	<0.001	<0.001
Ti	0.002	<0.001	<0.001	<0.001	0.001	<0.001	<0.001	<0.001	<0.001	<0.001
Zr position	0.998	1.004	1.008	1.001	1.002	1.003	1.000	1.007	1.001	1.003
Si	1.002	0.995	0.991	0.998	0.998	0.997	0.999	0.992	0.999	0.996

\* Including 0.17 wt% FeO and 0.09 wt% CaO

other zones including C with a yellowish-brownish coloration, the related zone in the {100} growth sector G, the Th-rich zone D, and the rim zone F with narrow growth zoning, the light REE are relatively depleted and heavy REE are strongly enriched as normally found in natural zircon and favored by the zircon structure (Speer, 1982).

Table 2 compiles U and Th contents defined by SHRIMP. One EMPA analysis from the Th-rich zone D is also included. The U and Th contents and Th/U ratios of 0.6 found in the core (zones A + B) are in a range typical of magmatic zircon from granitic rocks (*cf.* Ahrens, 1965; Ahrens *et al.* 1967; Hoskin & Ireland, 2000; Hoskin & Schaltegger, 2003). In the other zones, however, there is a strong increase in Th and Th/U ratios up to 6.500 ppm and 7.5, respectively, indicating that the core and the rest of the crystal may have a different origin. On the other hand, the transition between these two ranges is relatively smooth, hinting for a common origin of the whole crystal. The magmatic zircon from the host rock also displays enhanced Th/U ratios (2.3–3.9) at normal Th contents possibly reflecting the Th enrichment in the alkaline rocks.

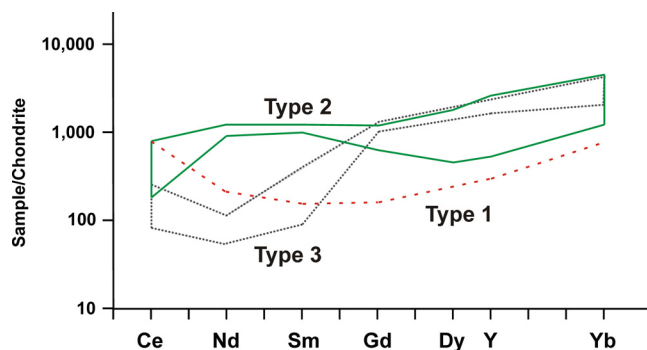


Fig. 5. REE+Y distribution patterns of yellowish hydrothermal zircon according to EMPA. Type 1 distribution is found in the greenish-yellowish core (analytical point 1 in Fig. 1b). Type 2 is typical of the rim zone of the core (point 2) and the zone preceding the oscillatory zoning at the rim (point 5). Type 3 distribution was found in the remaining zones (points 3, 4, 6, 7 and 8). Chondrite normalization according to Anders & Grevesse (1989) See text for discussion.

A conspicuous feature of the EMPA analyses of yellow zircon from the cavity are the low analytical totals ranging between 97.9 and 99.2 wt%. Totals for the wall-rock

Table 2. Contents of U and Th, U/Th ratios, calculated received radiation doses according to defined SHRIMP ages and line widths (FWHM) of the  $\nu_3$  ( $B_{1g}$ ) Raman mode fitted with a single line for Type 1 (hydrothermal) and Type 2 (magmatic) zircon from Mt. Malosa (Malawi).

Point	Hydrothermal Type 1						Magmatic Type 2		
	1	2	3	4* <sup>1</sup>	5	8	1	2	3
Element contents									
U	114	194	130	882	196	55	74	76	24
Th	67	110	393	6591	1452	176	291	230	55
Th/U	0.59	0.57	3.02	7.47	7.41	3.26	3.93	3.03	2.29
Calculated radiation dose									
(120 Ma)	0.05	0.09	0.09	0.96	0.21	0.04	0.06	0.05	0.01
(290 Ma)	0.13	0.20	0.21	2.34	0.52	0.09	0.14	0.12	0.04
Raman line broadening									
FWHM* <sup>2</sup>	6.2	13.9	18.1	20.3	13.4	19.2	3.7	3.4	2.9

U and Th in ppm. Dose in  $10^{18}$   $\alpha$ -events per g.

\*<sup>1</sup> Results for U and Th from EMPA.

\*<sup>2</sup> FWHM (in  $\text{cm}^{-1}$ ) of the  $\nu_3$  ( $B_{1g}$ ) Raman mode fitted with one band and corrected for apparatus function. The error from the fits is between  $\pm 1.2 \text{ cm}^{-1}$  (point 1) and  $\pm 3.8 \text{ cm}^{-1}$  (point 4) for Type 1 and  $\pm 0.8 \text{ cm}^{-1}$  for Type 2 zircon.

Table 3. Results of U–Pb SHRIMP analyses for Type 1 (yellowish hydrothermal) and Type 2 (brownish magmatic) zircon from Mt. Malosa (Malawi). Errors for calculated ages are one sigma. Th is calculated from the Th/U ratio.

Spot	U ppm	Th ppm	Th/U	Common Pb <sup>206</sup> %	<sup>238</sup> U/ <sup>206</sup> Pb uncorrected	<sup>207</sup> Pb/ <sup>206</sup> Pb uncorrected	<sup>206</sup> Pb/ <sup>238</sup> U age Ma ( <sup>204</sup> Pb corr.)	<sup>206</sup> Pb/ <sup>238</sup> U age Ma ( <sup>207</sup> Pb corr.)
Yellow hydrothermal zircon								
1	114	67	0.59	59.3	22.14 $\pm$ 0.35	0.4870 $\pm$ 0.0073		129.2 $\pm$ 4.5
2	194	110	0.57	14.9	50.46 $\pm$ 0.76	0.0867 $\pm$ 0.0024		120.5 $\pm$ 1.9
3	130	393	3.02	49.4	50.70 $\pm$ 1.00	0.0693 $\pm$ 0.0030		122.6 $\pm$ 2.5
5	196	1452	7.41	16.4	50.12 $\pm$ 0.80	0.0589 $\pm$ 0.0023		125.7 $\pm$ 2.1
8	54	176	3.26	91.0	48.10 $\pm$ 1.20	0.1288 $\pm$ 0.0067		119.2 $\pm$ 1.2
Brownish magmatic zircon								
1	74	291	3.93	4.5	21.53 $\pm$ 0.37	0.0536 $\pm$ 0.0020	279.7 $\pm$ 5.9	292.1 $\pm$ 4.8
2	76	230	3.03	3.1	21.34 $\pm$ 0.36	0.0607 $\pm$ 0.0021	292.1 $\pm$ 4.9	292.1 $\pm$ 4.9
3	24	55	2.29	6.1	22.01 $\pm$ 0.48	0.0587 $\pm$ 0.0033	269.5 $\pm$ 8.5	284.1 $\pm$ 6.3

zircon (99.4–99.7 wt%) and other zircons measured within the same session lie in the normal range between 99.5–100.1 wt%. The deficient results may be partly explained by the presence of other REE not measured during EMPA, especially La and Er. However, a calculation using the REE distribution patterns for rough estimation of the contents of all REE (excluding Eu) yields still too low analytical totals between 99.3 and 99.6 wt%. This phenomenon will be discussed in more detail below.

### 3.3. SHRIMP analysis and absolute age relations

The SHRIMP analysis was conducted to verify the age relationships between the two types of zircon and to obtain a data base for dosage calculations. The results are compared with the values obtained for birefringence and with data from EMP, Raman and CL measurements in one and the same crystal area. We have not aimed at a precise absolute age determination. Five points were analyzed in the hydrothermal zircon crystal from the cavity and three in the magmatic zircon from the wall rock. The results are listed in Table 3 and plotted in Fig. 6. Most of the

analytical points plot close to or on the Concordia. The data for the hydrothermal zircon are more discordant and there is considerable common lead which is an additional hint at its hydrothermal origin. If all five analytical points for this zircon are used for calculation without any assumptions for the composition of common lead, an age of  $122 \pm 2$  Ma (MSWD 1.7) can be obtained (Fig. 6). When the common lead composition is “anchored” according to the model by Stacey & Kramers at 0.83 <sup>207</sup>Pb/<sup>206</sup>Pb initial ratio, an age indistinguishable within error from the first one ( $125 \pm 7$  Ma; MSWD 1.8) is found. The Concordia age for the three most concordant points lies also in the same range ( $126 \pm 5$  Ma; MSWD 0.13). These data are in remarkable accordance with zircon ages reported by Högdahl & Jonsson (1999, 2002, cited in Soman *et al.*, 2010) and Soman *et al.* (2010) for zircon from the pegmatite cavities at Mt. Malosa ranging between  $117 \pm 1$  Ma and  $123 \pm 4$  Ma, and with the chemical age calculated by the latter authors for weakly altered thorite inclusions in zircon ( $122 \pm 5$  Ma). The K–Ar amphibole ages of  $111 \pm 3$  and  $115 \pm 3$  Ma reported earlier by Eby *et al.* (1995) are also similar though somewhat younger.

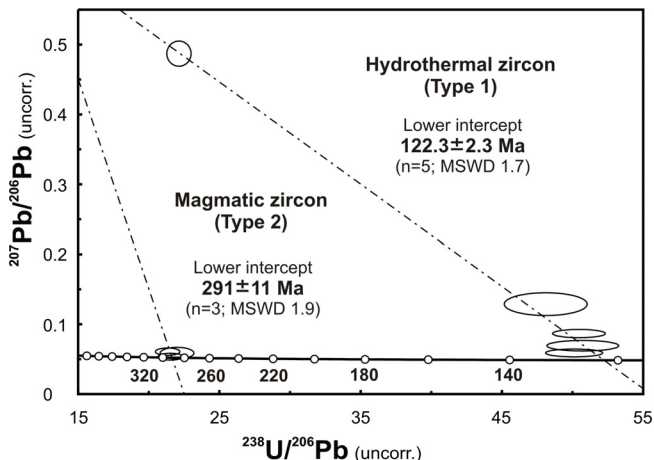


Fig. 6. Reverse Concordia plot of U–Pb SHRIMP data obtained for yellowish hydrothermal Type 1 zircon (crystal 1) and brownish magmatic Type 2 zircon from Mt. Malosa (Malawi). Error ellipses are two sigma. The strongly discordant point for Type 1 zircon corresponds to the core and displays high common Pb content. Nevertheless, calculations including or excluding this point with or without “anchored” common Pb composition yielded indistinguishable results for the calculated ages. See text for further discussion.

The few U–Pb data for the host-rock zircon studied here demonstrate that the formation age of that zircon and the related intrusion age of the granite should be significantly higher. The calculated U–Pb age for the crystal investigated is  $291 \pm 11$  Ma (MSWD 1.9; Fig. 6). The age data obtained for both zircon types were used for radioactive dose calculations listed in Table 2.

### 3.4. Raman spectroscopy

As in our previous study (Kempe *et al.*, 2010), all Raman measurements on the two sections of Type 1 zircon yielded spectra with significantly broadened Raman bands. Another, previously unnoted feature is the appearance of an appreciable asymmetry for the  $\nu_3$  ( $B_{1g}$ ) mode. The latter mode is commonly used to assess the degree of local disorder (Nasdala *et al.*, 1995, 2001, 2003). Significant asymmetry may also be seen for the neighboring  $\nu_1$  ( $A_{1g}$ ) mode (Fig. 7). As demonstrated in Fig. 7, it was commonly not possible to fit these two peaks adequately with one band, respectively. Some fitting results are listed in Table 2. In this table, band widths for yellow Type 1 zircon are given for a fit using only one band for each mode, respectively, in order to allow comparison to other work (*cf.* Palenik *et al.*, 2003). In the classical approach, such large Raman bandwidths (from  $6.2 \text{ cm}^{-1}$  in the core, but closer to the maximum value of  $20.3 \text{ cm}^{-1}$  in the rest of the crystal) clearly point to a high degree of radiation damage in the hydrothermal zircon. In contrast, Raman spectra of brownish Type 2 zircon show only very weak band broadening, typical of well-ordered zircon (Table 2).

Similar Raman measurements were conducted on the second sample of hydrothermal Type 1 zircon. Additionally,

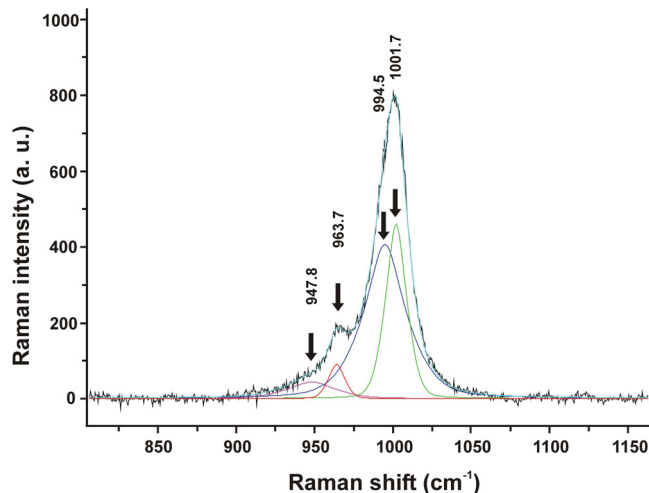


Fig. 7. Raman spectrum of yellowish hydrothermal Type 1 zircon with significant band asymmetry. Both the  $\nu_3$  ( $B_{1g}$ ) and  $\nu_1$  ( $A_{1g}$ ) modes cannot be adequately fitted with one band ( $999.7 \pm 0.8$  and  $967.2 \pm 1.1 \text{ cm}^{-1}$  with FWHM  $20.3 \pm 4.2$  and  $25.6 \pm 4.5 \text{ cm}^{-1}$ , respectively), especially at the peak flanks. This particular spectrum can be satisfactorily fitted with four bands (from the right to the left:  $1001.7 \pm 0.5$ , FWHM  $11.1 \pm 2.1$ ;  $994.5 \pm 0.5$ , FWHM  $24.0 \pm 2.8$ ;  $963.7 \pm 0.7$ , FWHM  $8.2 \pm 2.5$  and  $947.8 \pm 1.2$ , FWHM  $36.9 \pm 4.7 \text{ cm}^{-1}$ ). Note that despite the large uncertainties of the fit, the pairs of both modes at higher and lower wavenumbers show comparable bandwidths. The spectrum was taken in the area of point 5 in Fig. 1b. See text for further discussion.

two measurement series along profiles with a step width of  $10 \mu\text{m}$  were made. As shown below, these profiles crossed two types of internal textures revealed by OCI. Results for the fits of the Raman spectra are plotted in Fig. 8 and the locations of the profiles are marked in Fig. 9b. The Raman measurements in this second crystal were made after EBSD. One profile (number 2) was partly located inside an area studied by EBSD while the other probed a “pristine” region. In general, the Raman results for the second crystal were very similar to that for the first except that the bandwidths tend to be somewhat lower in the second crystal. When the  $\nu_3$  ( $B_{1g}$ ) mode is fitted with one band, the corrected FWHM varied between  $8.3$  and  $14.3 \text{ cm}^{-1}$ . However, the  $\nu_3$  ( $B_{1g}$ ) mode of all spectra could be successfully fitted only with two bands as in crystal 1. Fit results for the two profiles in Fig. 8 show that in the “pristine” area (profile 1), the behavior of both fitted bands is similar with a clear change both in line position and band width when crossing from one types of texture to the other, indicating more “disordered” states in the pronounced texture closer to the core. Changes in the band width of the higher frequency band are less well pronounced, however. In the second profile, the bands are moved to lower wavenumbers and the bandwidths are increased compared to profile 1. The texture closer to the core was additionally affected by EBSD. As can be seen from Fig. 8, the trend inside this area is not as clear as in profile 1. This result demonstrates the influence of electron irradiation

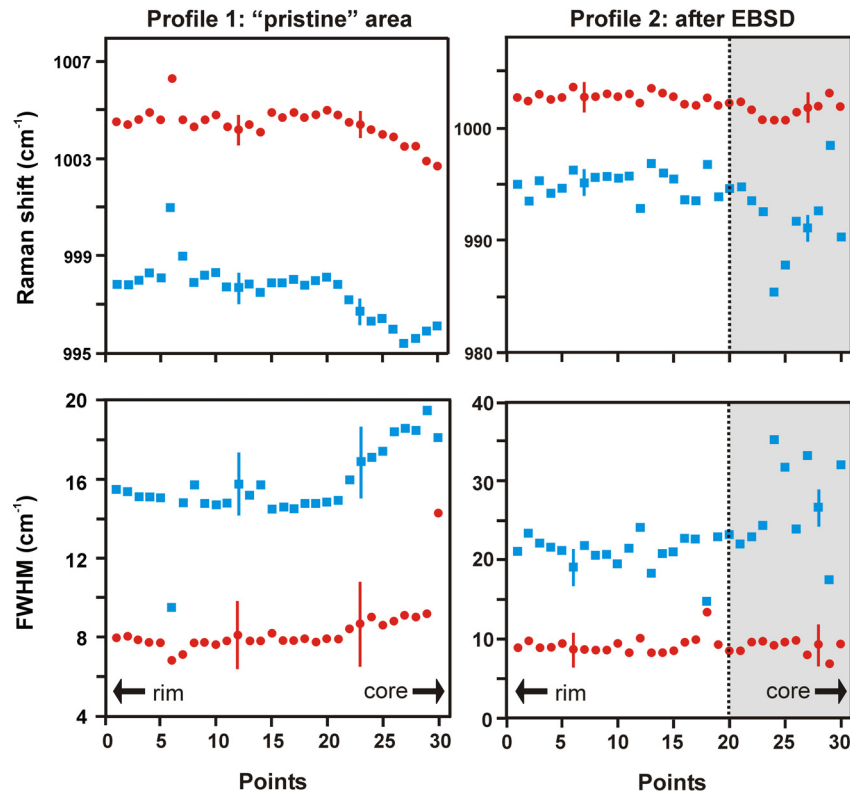


Fig. 8. Results of fits using two bands for the  $\nu_3$  ( $B_{1g}$ ) mode in the Raman spectra taken along two profiles in crystal 2 of yellowish hydrothermal zircon. Comparison of the area closer to the crystal core affected by previous EBSD analysis (shaded gray) in profile 2 (right) to profile 1 (left) demonstrates that the clear trend visible for the “pristine” area in profile 1 was distorted by the electron beam. Error bars defined for the fit are  $2\sigma$ . Locations of the profiles are shown in Fig. 9b.

(normally occurring at high doses during EMPA or EBSD because high beam currents focused in small spots are needed for these analyses) on the measured Raman characteristics of zircon. Similar effects were noted earlier by Nelson *et al.* (2000) and Nasdala *et al.* (2002b).

### 3.5. Orientation contrast imaging (OCI)

The OCI revealed a complex domain structure which shows no obvious relation to growth zoning visible in CL and BSE images (Fig. 9). The domain structure is well expressed in the central part of the crystal and weakens toward the prism faces and the crystal termination (Fig. 9b). Investigation with the cold field emission SEM revealed, however, that the domain structure is also present in these crystal areas (Fig. 9c), though it is not clearly discernible with conventional SEM (Fig. 9b). The domain size may reach several tens of micrometers. On the other hand, there is a “domain in domain” structure with the smallest visible domains measuring several dozens to hundreds of nanometers in size down to (or possibly below) the limit of resolution of the OC images (Fig. 9c). The orientation contrast commonly changes gradually within the domains, indicating high internal strain. In some places, domain walls are marked by abrupt contrast changes, which may be additionally outlined by cracks.

### 3.6. EBSD results

The location of the EBSD grids is shown in Fig. 10a. Two maps were obtained from the two areas shown in Fig. 9. Two additional areas were probed in the growth sector  $\{100\}$  and the Th-rich zone, respectively. The EBSD analysis shows that the observed OC is related to gradual changes in the lattice orientation as well as to abrupt changes at small angle boundaries (Fig. 10b and c). Note that indexing of EBSD patterns failed only in pits and cracks although the local resolution of the method is of the order of a few tens of nanometers, just in the range assumed for the extent of  $\alpha$ -recoil tracks in zircon (Ewing *et al.*, 2003). This result demonstrates that the long-range order in the crystal is well preserved. Misorientation angles at domain boundaries vary from the order of several tenths (mostly at the crystal termination) up to about  $10^\circ$  (in the central part of the crystal), occasionally reaching  $20^\circ$ . The main rotation axis may be defined along  $[013]$  with some orientation distribution around it. Orientation distribution is more clearly seen for rotation angles below  $5^\circ$ .

Band contrast (BC; height of the diffraction peaks above the background signal in the Hough space) varies in a similar manner as the orientation contrast in the OC images. In general, the BC depends on crystal perfection, phase orientation and several experimental parameters

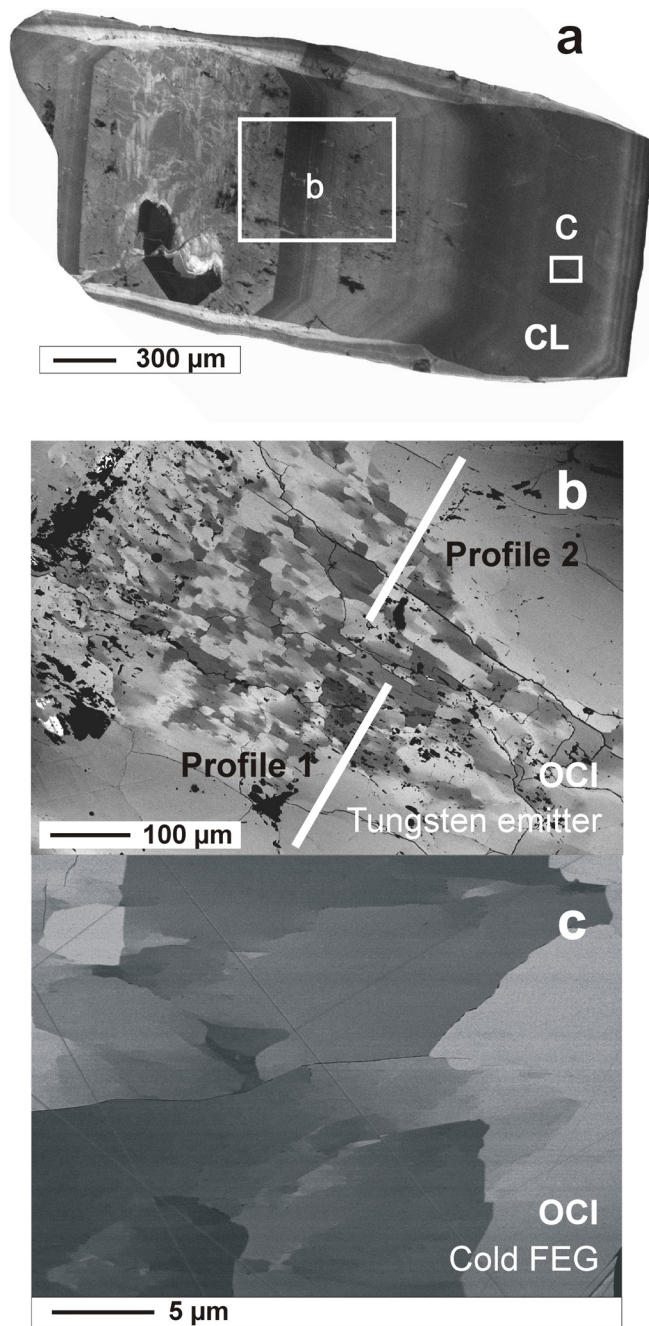


Fig. 9. Orientation contrast images (OCI) of the yellowish hydrothermal zircon (crystal 2): (a) CL image of the crystal with the location of the OCI (b and c). (b) OCI of a central region of the crystal obtained with conventional SEM (tungsten emitter). The locations of the two profiles investigated by Raman spectroscopy are marked on the figure. (c) OCI of a region closer to the crystal termination taken with a SEM equipped with a cold field emission gun and a large-angle BSE detector.

(Humphreys, 2001). Experimental parameters were kept constant in our case. The average BC value is the same in the central part of the crystal (map 1) and at the crystal termination (map 2) and in the other maps. On the other hand, variations in BC are much larger in the first case. We

may conclude that the long-range order is of about the same (high) degree in all areas probed and that variations in the BC are dominated by the orientation distribution.

The band slope (BS) parameter is determined by the width of the peaks in the Hough transform describing the maximum intensity gradient at the Kikuchi band margins. The band slope depends on the long-range order, crystallite size, internal strain and the same experimental parameters as BC. The BS parameter displays large variations in the central part of the crystal but only restricted distribution and higher average values at the crystal termination. Considering conclusions on BC, we interpret the variations in BS mainly as a result of distributions in internal strain and crystallite (domain) sizes rather than in long-range order.

## 4. Discussion

It is clear from the above results that the correlation between U and Th concentrations, age, birefringence, Raman spectroscopic behavior and structural changes normally reported for natural zircon and well explained by the radiation-damage model is not observed for the yellowish hydrothermal zircon from Malawi, although it holds for the well-ordered brownish magmatic zircon from the same rock sample. Several aspects of this apparent contradiction are discussed in more detail below.

### 4.1. Degree of disorder

The main problem arising with the interpretation of the data concerns the degree of disorder in the yellowish hydrothermal zircon. While a high degree of (short-range) disorder is indicated by Raman spectroscopy, birefringence suggests a high degree of short-range order (ordered orientation of covalent bonds) except for the Th-rich zones (Table 4). From dose calculations based on U + Th contents and U–Pb SHRIMP ages, only weak radiation damage is expected except for some enhanced values in the Th-rich zone (Table 4). No significant distortion of the long-range order is seen by EBSD in all areas investigated. We conclude from the data that there is a high degree of long-range order in both the magmatic and hydrothermal zircon crystals studied.

The Raman data, namely the FWHM defined for the  $\nu_3$  ( $B_{1g}$ ) mode fitted with a single band, may be plotted in a diagram together with the dose (calculated here from the SHRIMP data; Fig. 11) as proposed by Nasdala *et al.* (2001). The diagram shows that the disorder indicated by Raman spectroscopy for the hydrothermal zircon is much higher than can be expected from internal radiation in any realistic time interval considering the U and Th contents. All but one data point (calculated for an unrealistic high age) plot well above the linear array defined by Nasdala *et al.* (2001) as a calibration line for zircon samples with no evidence for annealing after crystallisation. Deviations from this line are frequently observed for zircon that experienced annealing well after formation. In this case,

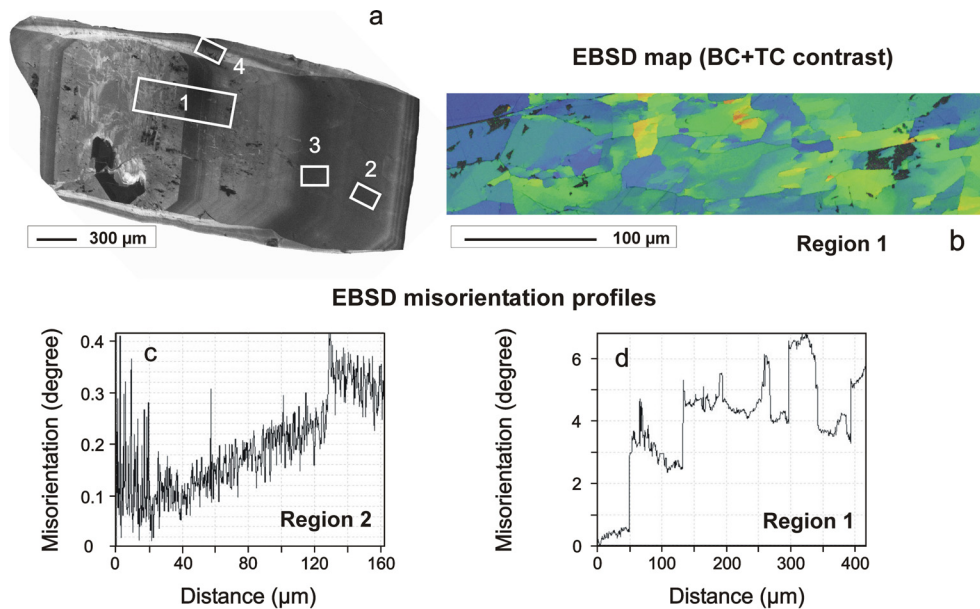


Fig. 10. Results of EBSD analysis of the yellowish hydrothermal zircon (crystal 2). (a) CL image of the crystal with the location of the mapped areas (1–4). (b) EBSD map of region 1 (band contrast + texture contrast) illustrating the orientation domain textures. (c) Misorientation profile through region 2. (d) Misorientation profile through region 1.

data points plot below the calibration line and projection on this line by recalculation to other ages is sometimes used to estimate the original dose and/or the (hydro-) thermal event responsible for recrystallisation (Nasdala *et al.*, 2001; Geisler *et al.*, 2003; Dziggel *et al.*, 2005; Tichomirowa *et al.*, 2005). However, this method is not applicable in our case. Other approaches are needed to explain the observed apparent discrepancies between the data obtained by various methods.

#### 4.2. BSE contrast and CL intensity

In an earlier work, we noted two types of zircon considering BSE and CL contrast: (1) “normal” zircon with inverse behavior of BSE and CL intensity and (2) zircon with low CL signal paralleled by “anomalous” low BSE (Kempe *et al.*, 2000). These relations were further explored by Nasdala *et al.* (2006, 2009). The cited authors found for zircon of the first type analytical totals close to 100 % (Nasdala *et al.*, 2009). Surprisingly, the BSE intensity was found to correlate well with the broadening of the Raman peaks in their samples rather than with the average atomic number as normally assumed in electron microscopy (Nasdala *et al.*, 2006). The zircon of the second type showed low analytical totals but there was no clear correlation with the Raman characteristics (Nasdala *et al.*, 2009). In our case, the brownish zircon from the host rock belongs to the first group – CL and BSE contrast are inversely correlated, the BSE signal is at a “normal” level and all microprobe analyses show good analytical totals. The Raman peaks are rather sharp. However, the yellowish hydrothermal zircon does not fit into a “two-type” schema. Except for the core region A in some crystals (*e.g.*, in crystal 1), the CL and BSE signals are inversely correlated,

but the analytical totals are always low when the trace-element content is high. In general, the BSE signal intensity in the crystals is at the same level as in the brownish zircon crystal (*i.e.* as in “common” zircon). The Raman peaks in the spectra from the yellowish zircon are always considerably broadened as further discussed below. The core region in the first crystal studied in more detail is somewhat similar to zircon of the second type characterised by Nasdala *et al.* (2009) because the CL is quenched while the BSE signal is low (Fig. 1) and Fe and Ca appear in detectable quantities (Table 1). This conclusion is also supported by SHRIMP analysis indicating high common lead (Table 3) and a significant discordance of the U–Pb system (Fig. 6).

#### 4.3. Element substitution, charge balance, stoichiometry, and analytical totals

A striking peculiarity of hydrothermal zircon from the cavity is the high contents of Y and the REE substituting for Zr as suggested by the microprobe analyses and formulae calculations shown in Table 1. It is well established that these elements substitute at the dodecahedral Zr site which is coordinated by eight oxygen atoms (Speer, 1982; Hoskin & Schaltegger, 2003). However, replacement of tetravalent Zr by trivalent Y and REE needs charge compensation. According to the literature, the most common compensation mechanism is the coupled substitution of P for Si in the tetrahedral site (see Speer, 1982; Finch *et al.*, 2001; Hoskin & Schaltegger, 2003 and Harley & Kelly, 2007 for summaries). This mechanism cannot be operative in our case because P could not be detected by EMPA. An alternative way of charge compensation is the coupled substitution of pentavalent

Table 4. Comparison of estimated doses (in  $10^{18}$   $\alpha$ -events per g) for hydrothermal (Type1) and magmatic (Type2) zircon from Malawi according to (1) chemical composition and age, (2) Raman spectroscopy using the linear array defined by [Nasdala \*et al.\* \(2001\)](#) in the plot FWHM for the  $\nu_3$  ( $B_{1g}$ ) Raman mode *vs.* dose calculated from chemical composition and age and (3) birefringence using the linear relation defined by [Palenik \*et al.\* \(2003\)](#) for Sri Lanka zircon.

Point	Dose calculated from age and U+Th (1)	Dose estimated from Raman spectroscopy (2)	Dose estimated from birefringence (3)
Yellowish hydrothermal Type 1 zircon (120 Ma)			
1	0.05	0.30	< 1.5
2	0.09	0.88	< 1.5
3	0.09	1.11	< 1.5
4	0.96	1.33	2.2–3.5
5	0.21	0.84	< 1.5
8	0.04	1.25	< 1.5
Brownish magmatic Type 2 zircon (290 Ma)			
1	0.14	0.14	< 1.5
2	0.12	0.12	< 1.5
3	0.04	0.07	< 1.5

(Note that the relationships obtained between calculated dose and Raman characteristics or birefringence, respectively, were originally not proposed for dose calculations. This is because such relationships would apply only for cases when the thermal history of the measured and the reference samples was the same after crystal formation. In the case of Raman, the linear array applies for zircon not re-heated after formation ([Nasdala \*et al.\*, 2001](#)) as found for magmatic zircon in our case. The linear relationship found for birefringence rests on measurements on Sri Lanka samples certainly re-heated after formation. See text for further explanations.)

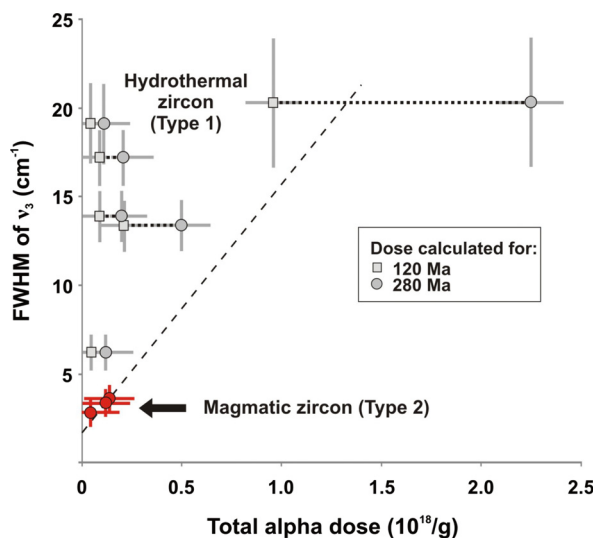


Fig. 11. Plot of the FWHM of the  $\nu_3$  ( $B_{1g}$ ) mode in the Raman spectra *versus* dose calculated from SHRIMP data (*cf.* [Table 2](#)) according to [Nasdala \*et al.\* \(2001\)](#). For hydrothermal zircon, doses for both U–Pb SHRIMP ages (120 and 280 Ma) were calculated and plotted in the figure. The points of the magmatic zircon calculated for an age of 280 Ma plot on the calibration line defined by [Nasdala \*et al.\* \(2001\)](#) for zircons not annealed after formation.

Nb and Ta for tetravalent Zr and Hf ([Vinokurov \*et al.\*, 1964](#); [Solntsev & Shcherbakova, 1974](#); [Di Gregorio \*et al.\*, 1980](#); [Speer, 1982](#); [Smith \*et al.\*, 1991](#); [Hoskin & Schaltegger, 2003](#)). Although Nb is present in measurable quantities in the zircon studied, the content is too low to compensate the charge unbalance from Y and the REE (see [Table 1](#)). A third possibility of charge compensation often overlooked is incorporation of pentavalent U at the zirconium position known from doping experiments ([Vance & Mackey, 1978](#)). The presence of pentavalent

U in natural zircon is well established by absorption spectroscopy in the near-IR range ([Vance & Mackey, 1974](#); [Zhang \*et al.\*, 2003](#)). In our case, however, the U content is also by far too low to account for compensation although the lack of  $U^{4+}$  lines in the optical absorption spectra and of  $UO_2^{2+}$  in the luminescence spectra suggests that nearly all U in this zircon is present in the pentavalent state. Other suggestions for charge compensation not applicable in our case were reviewed by [Speer \(1982\)](#) and [Smith \*et al.\* \(1991\)](#) and include charge compensation by divalent elements (Ca, Fe) or by Al, replacement of oxygen by hydroxyl groups and formation of holes trapped on oxygen. Note that no water or OH could be found by Raman spectroscopy in our case. [Finch \*et al.\* \(2001\)](#), [Ushikubo \*et al.\* \(2008\)](#) and [Soman \*et al.\* \(2010\)](#) showed or assumed that Li is a possible compensator. It is still unclear which position Li should take in the zircon structure and we have no hints for Li mineralization at our sampling location as stated above. Note, however that Li is frequently present in enhanced concentrations in Zr–Nb–REE mineralisation. In the case of the Jack Hills zircon studied by [Ushikubo \*et al.\* \(2008\)](#), the Li was found in zircon in alteration zones apparently formed during weathering. Lithium together with P could not maintain charge balance in that case. Lithium was also noted by [Smith \*et al.\* \(1991\)](#) in zircon from Thor Lake (Canada) where its content has also been estimated to be too low for charge compensation. Although we assume that Li does not fit well into the zircon structure, the role of Li in zircon merits further investigation.

Summarising, charge unbalance from trivalent elements replacing Zr and Hf is apparently not compensated by coupled substitution with other cations in our zircon. In a comprehensive study on zircon from various localities in the Alps, [Rizzo \*et al.\* \(2000\)](#) have also found a significant number of cases, where Y+REE substitution was not

compensated by P or other elements measured. They concluded that significant distortions in the mineral structure should result. We assume here, considering the absence of measurable F, that one possible explanation is charge compensation by oxygen vacancies, a mechanism widely unnoticed or neglected (Finch *et al.*, 2001) in the literature.

There are also hints for further deviations from the ideal structure which cannot be, however, proven here due to the low precision level of the microprobe analysis. All non-formula elements detected (including U, Th and Ti; Solntsev & Shcherbakova, 1972; Speer, 1982; Harley & Kelly, 2007) substitute for Zr and Hf. It is, therefore, interesting to look whether or not stoichiometry is maintained between the Si and Zr sites. Apparently, there is a tendency for an increased deviation from stoichiometry with increasing contents of trivalent elements (Fig. 12). If this is not related to an analytical artefact (*e.g.*, to a systematic overestimation of the Y content for what we have presently no hint) this deviation from stoichiometry indicates the occurrence of some additional vacancies on the tetrahedral (Si) position which, in turn, should result in an increasing number of oxygen vacancies for charge compensation. Interestingly, similar non-stoichiometry effects were noted by Finch *et al.* (2001) for synthetic crystals doped with REE and P. We have noted earlier another type of deviation from zircon stoichiometry observed for Hf-rich zircon with an anomalous low BSE contrast and with low contents of other non-formula elements. In that case, reversely, a deficit on the Zr position was apparent (Kempe *et al.*, 1997).

As shown above, our analyses of the Y- and REE-rich zircon yielded analytical totals below 100 wt%. Similar low totals for trace-element rich zircon were reported by Černý & Siivola (1980) and Pointer *et al.* (1988) for hydrothermally altered zircon from the Tanco pegmatite (Canada) and the Ririwai granite (Nigeria), respectively, and by Smith *et al.* (1991) for hydrothermal zircon from Thor Lake (Canada). These authors assumed an additional presence of “water” and a role of sub-microscopic voids in their samples.

The problem of low analytical totals frequently met for natural zircon was explored by Pointer *et al.* (1988), Smith *et al.* (1991), Pérez-Soba *et al.* (2007) and is recently reviewed and further evaluated by Nasdala *et al.*, (2009, 2010). The conclusion by the first two authors favouring the incorporation of water or OH groups and/or the existence of sub-microscopic voids was corroborated by the data obtained by the latter authors. According to these models, voids and possible water uptake occur in zircon by recrystallisation of metamict crystal areas during hydrothermal alteration. In our case, however, low analytical totals cannot be explained by sub-microscopic voids partly filled with water. Although there are areas in the investigated crystals rich in such voids down to a few hundreds of nanometres or less in diameter which are often observed in high-resolution FE SEM imaging, large parts of the crystals lack such voids. No systematic relation between low analytical totals and the appearance of voids

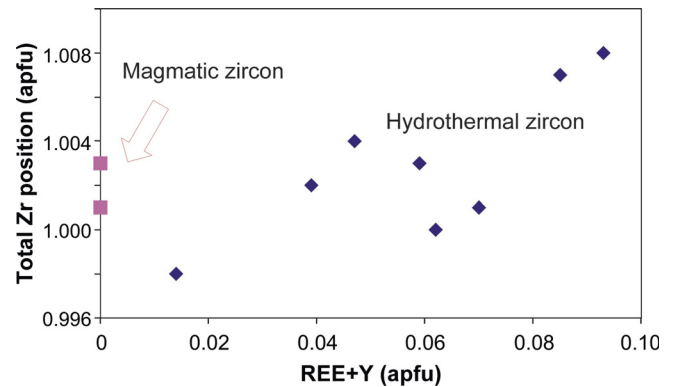


Fig. 12. Evaluation of results of EMPA (data from Table 1): comparison of apparent site occupancy on the Zr position with the content of REE + Y.

in the respective areas could be found. In general, areas with voids were avoided during our EMPA and SHRIMP measurements. This point merits further research.

#### 4.4. Interpretation of Raman spectra

The original interpretation of line broadening and shift in the Raman spectra of zircon was based on the observation that changes in the spectra may be correlated with similar changes in the position and line widths in X-ray powder diffraction patterns measured for the same samples (Nasdala *et al.*, 1995). The weakness of this approach was in its purely empirical nature. In a later discussion, Nasdala *et al.* (2002a) suggested that line broadening observed for the internal  $\nu_3$  vibration results from irregular distortion and tilting of individual  $[\text{SiO}_4]$  tetrahedra resulting from strain induced by point defects (produced by radioactive irradiation) and from the presence of an amorphous phase, while the Raman band shift reflects the lattice expansion established by XRD analysis. Similar conclusions were reached earlier by Woodhead *et al.* (1991) applying IR analysis and by Knittel & Williams (1993) after high-pressure Raman experiments, but they are in conflict with an XRD single-crystal study on moderately metamict zircon that demonstrated that changes in the  $[\text{SiO}_4]$  tetrahedra are negligible (Ríos *et al.*, 2000a).

As revealed by OCI and EBSD, the Raman laser probed heterogeneous crystal areas (domains) of the hydrothermal zircon from Malawi with distribution of (1) lattice orientation, (2) domain sizes, and (3) internal strain. In general, Raman spectra may be affected by all three factors (Burns & Scott, 1970; Sanjurjo *et al.*, 1983; Frey & Payne, 1996). However, orientation distribution cannot be accounted for band shifts here because Raman-active modes in zircon are not polarized. The influence from phonon confinement effects within the domains should also be negligible because the domain sizes are mainly well above the critical value of 20–30 nm (*e.g.*, Nasdala *et al.*, 2002a). We propose that the variations in the Raman spectra may be directly linked to internal strain, an effect well known from other crystalline materials (*e.g.*, De Wolf *et al.*, 1992). In this interpretation, the direction and extent of the line shifts are a measure of the kind and extent of the

strain while the line widths characterise strain distribution. As shown by De Wolf *et al.* (1992), tensional strain occurring *e.g.* at grain boundaries causes mainly line shifts to lower frequencies while compression shifts the lines to higher values excluding for “soft” modes. Shifts of Raman lines to higher values related to compression were previously reported from high-pressure experiments on zircon (Knittel & Williams, 1993; Nasdala *et al.*, 2008) and for zircon enclosed in sapphire (Wang *et al.*, 2006). We further note that changes in the band position and widths are also observed for external (lattice related) modes and are not restricted to the internal modes of the [SiO<sub>4</sub>] tetrahedron (see also Nasdala *et al.*, 1995). We may conclude that line shifts to lower Raman frequencies observed in our case reflect tensional strain in the hydrothermal zircon under consideration as suggested by OC imaging and EBSD.

The internal tension may be explained in several ways. At least in part, the strain is simply related to the substitution of larger elements into the Zr site (Solntsev & Shcherbakova, 1974; Hoskin & Black, 2000; Finch *et al.*, 2001).

The influence of substitution into the Zr site on the Raman spectra of synthetic zircon was studied for the cases of Hf, Y and U by Hoskin & Rodgers (1996), Nasdala *et al.* (2003) and by Geisler *et al.* (2005) for Chernobyl “lava” zircon, respectively. For Hf, a weak increase in the Raman shift for internal stretching modes and some decrease for internal rotational and external modes was observed. No significant changes in the line widths were reported (Hoskin & Rodgers, 1996). Substitution of Y or U causes an increase in band widths and the occurrence of band asymmetry (Nasdala *et al.*, 2003) as well as a shift to lower wavelength numbers (Geisler *et al.*, 2005). Note, however, that the maximum spectral changes observed in synthetic zircon, even for a substitution of about 12 mol % USiO<sub>4</sub> as for the U-rich Chernobyl zircon, are well below the changes found in our study. To give an example, the FWHM in the U-rich Chernobyl zircon approaches 6.7 cm<sup>-1</sup> for the  $\nu_3$  (B<sub>1g</sub>) mode, while up to 20.3 cm<sup>-1</sup> were found for Malawi zircon. We assume that the effect of line shift and broadening is further enhanced by vacancy formation and the problem to compensate for these structural changes by ordering processes, twinning etc. promoting local strain domain formation. Note that the zircon structure is very rigid as reflected by the unusually low thermal expansion and compressibility of zircon (Özkan & Jamieson 1978; Hazen & Finger, 1979; Speer & Cooper, 1982).

Reddy *et al.* (2006, 2009) assigned similar internal textures detected by EBSD to deformation events induced by external stress. Growth in open space and lack of any signs of deformation preclude such an interpretation in our case. Summarizing, we favour internal (structural) mechanisms to be responsible for the occurrence of tensional strain.

The suggestions made here on the role of internal strain are corroborated by the results obtained from the Raman measurements along the two profiles crossing two textural areas of orientation distribution in the second crystal

(Fig. 8 and Fig. 9b). The extent of domain misorientation measured by EBSD correlates with the extent of assumed tension and strain distribution indicated by the Raman spectra. Partial relaxation of strain between the two areas seen in the Raman spectra after intense electron irradiation during EBSD analysis (Fig. 8) may be explained by local heating effects and by electron trapping in the zircon structure, namely, oxygen vacancies can act as excellent electron traps.

Remarkably, the observed domain structure with related tensional strain distribution may also explain the band asymmetry observed in the Raman spectra. As shown above, the resolution of Raman spectroscopy and the domain sizes are of comparable order. That means that two or more domains may be present within a single Raman spot. The resulting effect leading to the appearance of asymmetric Raman bands in the spectra was earlier demonstrated by Nasdala *et al.* (2005) by an intentional measurement on a boundary between two areas with quite different degrees of metamictization in a single zircon grain. The asymmetry may be also related to strain distribution within single domains.

No asymmetry was observed in our previous study on single crystals of hydrothermal zircon from the Malawi sample (Kempe *et al.*, 2010). In that work, the volume probed by the Raman measurements was further enlarged by focusing the laser beam below the sample surface with a resulting signal averaged over a much greater number of domains. We assume that high statistics in strain distribution yielded symmetric broad bands in the resulting composite spectra.

Note that in a conventional study, the Raman spectroscopy of the hydrothermal zircon from Malawi would suggest a high degree of metamictization. Such samples are commonly avoided in geochronological studies. However, no general analytical problems except enhanced contents of common lead were met during our SHRIMP analysis.

#### 4.5. CL spectroscopy

While the CL spectra of the magmatic zircon reflect the well-ordered structural state of this zircon with common broad-band emissions accompanied by some weak line emissions related to the REE<sup>3+</sup>, the CL spectroscopy of the yellow hydrothermal zircon underlines its unusual character. The strong REE<sup>3+</sup> line emissions correspond to the high contents of the REE in the crystals. Remarkably, there are crystal areas with even more intense emissions from the light REE than from the heavy one. Comparable intense Nd<sup>3+</sup> emission were not yet reported in the literature for natural zircon. Note that heavy REE fit easier into the zircon structure than light REE. Accordingly, higher local distortion may be expected from the very high light-REE contents. On the other hand, comparison of the Dy<sup>3+</sup> emission in well-ordered brownish magmatic zircon and in the yellowish hydrothermal one does not show any significant line broadening (*cf.* Fig. 3 and Fig. 4). Although this may be related to some extent to the resolution of the fine structure in our spectra, this observation may also

indicate preservation of long-range order (resulting in only weak variations in the crystal field around the REE) in the hydrothermal zircon despite significant substitution of non-formula elements (*cf.* Lenz *et al.*, 2013; Lenz & Nasdala, 2015). However, the more sensitive, common broad-band emissions related to the defect structure in well-ordered zircon (Kempe *et al.*, 2000, 2010) are completely absent in the hydrothermal zircon indicating that some kind of disorder should be present. We assume here that the quenching of intrinsic broad band luminescence results mainly from the high vacancy concentration discussed above.

#### 4.6. Possible consequences for the model of zircon metamictization

Although the yellowish hydrothermal zircon discussed above is certainly a very rare and extreme case, we assume that our findings may also contribute to the general understanding of the phenomenon of disorder in zircon and zircon metamictization. Besides the accepted model assuming radioactive decay as the leading process, there may be other mechanisms operative and resulting in the effects observed. One assumption made previously for metamict minerals in general was that metamictization may be related to the formation of very small, metastable and partially ordered domains with high defect densities within the crystals which show a misorientation distribution (Pyatenko, 1970; Graham & Thornber, 1974, 1975). The formation of such domains may or may not be accelerated by radioactive irradiation. It was further assumed that the formation of such domains may be induced by a complex composition, substitution of large cations and/or charge unbalances (Aleksandrov, 1960; Graham & Thornber, 1974). Note that metamictization most often occurs in complex oxides where ordering processes are complicated by the complex chemical composition and in structures with highly charged cations (Graham & Thornber, 1974, 1975). Meldrum *et al.* (1999) noted as a result of TEM investigations on zircon that a polycrystalline structure is observed in natural metamict zircon which is not reproduced by ion irradiation. Slightly misoriented microcrystallites about 100 nm in size were also found by Bursill & McLaren (1966) in a TEM study on another metamict zircon. In Fig. 13, we compare the orientation distribution in the EBSD pole figure [1 0 0] of our Malawi sample with the orientation distribution reported by Ríos & Salje (1999) for diffuse X-ray scattering of the (4 0 0) reflection in the reciprocal space of a slightly metamict sample from Moroto (Uganda). The similarity is striking. The latter authors explained their results by an intrinsic mosaic of the sample and swelling of defective areas.

Note that according to our interpretation of the line broadening and shift, Raman spectroscopy of partly metamict zircon indicates always tensional strain for the damaged and undamaged crystalline parts present there along with amorphous regions, according to the accepted model for zircon amorphization (see Chakoumakos *et al.*, 1987; Salje *et al.*, 1999; Zhang *et al.*, 2000). In contrast,

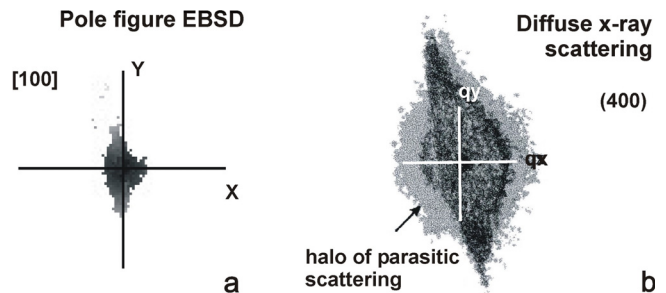


Fig. 13. Similarity in orientation distribution of (a) domains in the hydrothermal zircon from Malawi illustrated by the central part of the [1 0 0] EBSD pole figure (this work) and (b) for Moroto zircon (Ríos & Salje, 1999) illustrated by diffuse X-ray scattering of the (4 0 0) reflection in the reciprocal space.

compression is expected according to the amorphization model in highly metamict zircon when the volume swelling is mainly related to the volume increase by formation of amorphous regions (Weber & Maupin, 1988), *i.e.* beyond the second percolation point (Salje *et al.*, 1999).

In conclusion of this discussion, we would stress the convergence between both mechanisms of amorphization, namely complex substitution and radioactive irradiation, because the  $\alpha$ -recoil during the decay of U and Th produces mostly oxygen vacancies (Bursill & McLaren, 1966; Park *et al.*, 2001; Ewing *et al.*, 2003) which are responsible for strain and misorientation distribution in the present case of the Malawi zircon. In the Malawi zircon, however, oxygen vacancies were rather formed by charge compensation for trivalent elements substituting into the zirconium site.

#### 4.7. Hydrothermal activity and cooling history of the Mt. Malosa complex

Our results may also shed some light on the magmatic and hydrothermal history of the Mt. Malosa complex. Although more geochronological work is needed, the age defined for the apparently magmatic zircon in our sample indicates that alkaline magmatism at least in the Zomba-Malosa massif may be significantly older than previously assumed (Eby *et al.*, 1995). As a consequence, K–Ar ages for amphibole and fission track ages for apatite and zircon reported by the latter authors may reflect hydrothermal reset ages rather than cooling ages.

### 5. Conclusion

The example of the unusual hydrothermal zircon from Mt. Malosa, Malawi suggests that Raman spectroscopy of partly or strongly disordered zircon may reflect internal strain due to misorientation domain structures of variable size. Changes in the spectra may not directly be linked to the damage of the long- and short-range order in the crystal caused by radioactive irradiation. This fact again raises the problem of the nature of the disorder frequently observed in natural zircon.

**Acknowledgements:** The authors thank Andreas Massanek (Freiberg) for providing access to samples from Malawi including the studied sample, Freiberg Mineral Collection #80504. Michael Magnus (Freiberg) is thanked for excellent preparation of the EBSD section and Dieter Dettmar (Bochum) for his efforts with the preparation of oriented thin sections of zircon crystals. We are indebted to Rune Gehrlein for providing access to the EBSD Oxford Instruments demonstration facility in Wiesbaden. Shunsuke Asahina (JEOL Europe) assisted with sample preparation for OC imaging and operation of the JSM 7500F. Dieter Rhede (Potsdam) carried out electron probe microanalyses. The manuscript greatly benefited from critical comments on earlier versions by Steve Reddy and Marion Tichomirowa and from careful examination by two anonymous reviewers. S.V. Krivovichev is thanked for his editorial efforts.

## References

- Ahrens, L.H. (1965): Some observations on the uranium and thorium distributions in accessory zircon from granitic rocks. *Geochim. Cosmochim. Acta*, **29**, 711–716.
- Ahrens, L.H., Cherry, R.D., Erlank, A.J. (1967): Observations on the Th-U relationship in zircons from granitic rocks and from kimberlites. *Geochim. Cosmochim. Acta*, **31**, 2379–2387.
- Akhmatova, M.V. & Leonova, L.L. (1961): Study of metamict decay of zircon using infrared absorption spectra. *Geokhimiya*, **5**, 401–414 (in Russian).
- Aleksandrov, V.B. (1960): Crystal structure of fersmite. *Dokl. Akad. Nauk SSSR*, **132**, 669–672 (in Russian).
- Anderson, A.J., Wirth, R., Thomas, R. (2008): The alteration of metamict zircon and its role in the remobilization of high-field-strength elements in the Georgeville granite, Nova Scotia. *Can. Mineral.*, **46**, 1–18.
- Anders, E. & Grevesse, N. (1989): Abundances of the elements: meteoric and solar. *Geochim. Cosmochim. Acta*, **57**, 197–214.
- Bau, M. (1996): Controls on the fractionation of isovalent trace elements in magmatic and aqueous systems: Evidence from Y/Ho, Zr/Hf, and lanthanide tetrad effect. *Contrib. Mineral. Petrol.*, **123**, 323–333.
- Black, L.P., Kamo, S.I., Allen, C.M., Aleinikoff, J.M., Davis, D.W., Korsch, R.J., Foudoulis, C. (2003): TEMORA 1: a new zircon standard for Phanerozoic U-Pb geochronology. *Chem. Geol.*, **200**, 155–170.
- Bruneel, J.L., Lassègues, J.C., Sourisseau, C. (2002): In-depth analyses by confocal Raman microspectrometry: experimental features and modelling of the refraction effects. *J. Raman Spectr.*, **33**, 815–828.
- Burns, G. & Scott, B.A. (1970): Raman spectra of polycrystalline solids; application to the  $\text{PbTi}_{1-x}\text{Zr}_x\text{O}_3$  system. *Phys. Rev. Lett.*, **25**, 1191–1194.
- Bursill, L.A. & McLaren, A.C. (1966): Transmission electron microscope study of natural radiation damage in zircon ( $\text{ZrSiO}_4$ ). *Phys. Stat. Solidi*, **13**, 331–343.
- Černý, P. & Siivola, J. (1980): The Tanco pegmatite at Bernic Lake, Manitoba. XII. Hafnian zircon. *Can. Mineral.*, **18**, 313–321.
- Cesbron, F., Blanc, P., Ohnenstetter, D., Remond, G. (1995): Cathodoluminescence of rare earth doped zircons. I Their possible use as reference materials. *Scann. Micr. Suppl.*, **9**, 35–56.
- Chakoumakos, B.C., Murakami, T., Lumpkin, G.R., Ewing, R.C. (1987): Alpha-decay-induced fracturing in zircon: The transition from the crystalline to the metamict state. *Science*, **236**, 1556–1559.
- Chakoumakos, B.C., Oliver, W.C., Lumpkin, G.R., Ewing, R.C. (1991): Hardness and elastic modulus of zircon as a function of heavy-particle irradiation dose: I. *In situ*  $\alpha$ -decay event damage. *Rad. Eff. Def. Sol.*, **118**, 393–403.
- Davis, D.W., Williams, I.S., Krough, T.E. (2003): Historical development of zircon geochronology. in “Zircon”, J.M. Hanchar & P.W.O. Hoskin, ed. Reviews in Mineralogy and Geochemistry, 53, Mineralogical Society of America, Washington D.C., 145–181.
- Delines, M., Delhal, J., Tarte, P. (1977): Metamictization and U-Pb systematic – a study by infrared absorption spectrometry of Precambrian zircons. *Earth Planet. Sci. Lett.*, **33**, 331–344.
- De Wolf, I., Vanhellermont, J., Romano-Rodriguez, A., Norström, H., Maes H.E. (1992): Micro-Raman study of stress distribution in local isolation structures and correlation with transmission electron microscopy. *J. Appl. Phys.*, **71**, 898–906.
- Di Gregorio, S., Greenblatt, M., Pifer, J.H. (1980): ESR of  $\text{Nb}^{4+}$  in zircon. *Phys. Stat. Solidi (b)*, **101**, K147–K150.
- Dingley, D. (2004): Progressive steps in the development of electron backscatter diffraction and orientation imaging microscopy: *J. Micr.*, **213**, 214–224.
- Dziggel, A., Armstrong, R.A., Stevens, G., Nasdala, L. (2005): Growth of zircon and titanite during metamorphism in the granulite-gneiss terrane south of the Barberton greenstone belt, S Afr. *Mineral. Mag.*, **69**, 1019–1036.
- Eby, G.N., Roden-Tice, M., Krueger, H.L., Ewing, W., Faxon, E.H., Woolley, A.R. (1995): Geochronology and cooling history of the northern part of the Chilwa Alkaline Province, Malawi. *J. Afr. Earth Sci.*, **20**, 275–288.
- Everall, N.J. (2000): Modelling and measuring the effect of refraction on the depth resolution of confocal Raman microscopy. *Appl. Spectr.*, **54**, 773–782.
- Ewing, R.C. (2001): The design and evaluation of nuclear waste forms: clues from mineralogy. *Can. Mineral.*, **39**, 697–715.
- Ewing, R.C., Lutze, W., Weber, W.J. (1995): Zircon: A host-phase for the disposal of weapons plutonium. *J. Mater. Res.*, **10**, 243–246.
- Ewing, R.C., Meldrum, A., Wang, L.M., Weber, W.J., Corrales, L.R. (2003): Radiation effects in zircon. in “Zircon”, J.M., Hanchar & P.W.O. Hoskin, ed. Reviews in Mineralogy and Geochemistry, 53, Mineralogical Society of America, Washington D.C., 387–425.
- Finch, R.J., Hanchar, J.M., Hoskin, P.W.O., Burns, P.C. (2001): Rare-earth elements in synthetic zircon: Part 2. A single-crystal X-ray study of xenotime substitution. *Am. Mineral.*, **86**, 681–689.
- Finch, A.A., Garcia-Guinea, J., Hole, D.E., Townsend, P.D., Hanchar, J.M. (2004): Ionoluminescence of zircon: rare earth emissions and radiation damage. *J. Phys. D: Appl. Phys.*, **37**, 2795–2803.
- Frey, M.H. & Payne, D.A. (1996): Grain-size effect on structure and phase transformations for barium titanate. *Phys. Rev. B*, **54**, 3158–3168.
- Friis, H., Finch, A.A., Williams, C.T., Hanchar, J.M. (2010): Photoluminescence of zircon ( $\text{ZrSiO}_4$ ) doped with  $\text{REE}^{3+}$  ( $\text{REE} = \text{Pr, Sm, Eu, Gd, Dy, Ho, Er}$ ). *Phys. Chem. Minerals*, **37**, 333–342.

- Gaft, M., Panczer, G., Reinfeld, R., Shinno, I. (2000): Laser-induced luminescence of rare-earth elements in natural zircon. *J. All. Comp.*, **300–301**, 267–274.
- Geisler, T., Burakov, B.E., Zirlin, V., Nikolaeva, L., Pöml, P. (2005): A Raman spectroscopic study of high-uranium zircon from the Chernobyl “lava”. *Eur. J. Mineral.*, **17**, 883–894.
- Geisler, T., Rashwan, A.A., Rahn, M., Poller, U., Zwingmann, H., Pidgeon, R.T., Schleicher, H., Tomaschek, F. (2003): Low-temperature hydrothermal alteration of natural metamict zircons from the Eastern Desert, Egypt. *Mineral. Mag.*, **67**, 485–508.
- Gentry, R.V., Sworski T.J., McKown, H.S., Smith, D.H., Eby, R.E., Christie, W.H. (1982): Differential lead retention in zircons: Implications for nuclear waste containment. *Science*, **216**, 296–298.
- Graham, J. & Thornber, M.R. (1974): The crystal chemistry of complex niobium and tantalum oxides. IV. The metamict state. *Am. Mineral.*, **59**, 1047–1050.
- , — (1975): The crystal chemistry of complex niobium and tantalum oxides. IV. The metamict state: Reply. *Am. Mineral.*, **60**, 734.
- Guastoni, A. & Pezzotta, F. (2007): REE-mineral phases replacing helvite, niobian-rutile, bastnäsite-(Ce) from alkaline pegmatites of Mount Malosa, Zoma District, Malawi. in “Granitic pegmatites: The state of the art”, International Symposium, Porto, Portugal (abstract), 42–43.
- Guastoni, A., Nestola, F., Giaretta, A. (2009): Mineral chemistry and alteration of rare earth element (REE) carbonates from alkaline pegmatites of Mount Malosa, Malawi. *Am. Mineral.*, **94**, 1216–1222.
- Harley, S.L. & Kelly N.M. (2007): Zircon tiny but timely. *Elements*, **3**, 13–18.
- Hazen, R.M. & Finger, L.W. (1979): Crystal structure and compressibility of zircon at high pressure. *Am. Mineral.*, **64**, 196–201.
- Högdahl, K. & Jonsson, E. (1999): Age and mineral assemblages in agpaite pegmatites in the Chilwa alkaline province, Malawi, SE Africa. *J. Conf. Abstr.*, **4**, 767
- Högdahl, K. & Jonsson, E. (2002): CL characteristics versus Th, U, Hf contents in alkaline pegmatite-hosted zircon. in “The 25th Nordic geological winter meeting”, S.S. Jonsson, ed. Reykjavik (Abstract), 27.
- Holland, H.D. & Gottfried D. (1955): The effect of nuclear radiation on the structure of zircon. *Act. Crystallogr.*, **8**, 291–300.
- Hoskin, P.W.O. & Black, L.P. (2000): Metamorphic zircon formation by solid-state recrystallization of protolith igneous zircon. *J. metamorphic Geol.*, **18**, 423–439.
- Hoskin, P.W.O. & Ireland, T.R. (2000): Rare earth element chemistry of zircon and its use as a provenance indicator. *Geology*, **28**, 627–630.
- Hoskin, P.W.O. & Rodgers, K.A. (1996): Raman spectral shift in the isomorphous series  $(Zr_{1-x}Hf_x)SiO_4$ . *Eur. J. Solid State Inorg. Chem.*, **33**, 1111–1121.
- Hoskin, P.W.O. & Schaltegger, U. (2003): The composition of zircon and igneous and metamorphic petrogenesis. in “Zircon”, J.M. Hanchar, P.W.O. Hoskin, ed. Reviews in Mineralogy and Geochemistry, 53, Mineralogical Society of America, Washington D.C., 27–62.
- Humphreys, F.J. (2001): Grain and subgrain characterisation by electron backscatter diffraction. *J. Mat. Sci.*, **36**, 3833–3854.
- Iacconi, P. (1995): Thermoluminescence of zircon. *Scan. Micr. Suppl.*, **9**, 13–34.
- Iacconi, P. & Caruba, R. (1980): Trapping and emission centres in X-irradiated zircon. III. Influence of trivalent rare-earth impurities. *Phys. Stat. Solidi (a)*, **62**, 589–596.
- Karali, T., Can., N., Townsend, P.D., Rowlands, A.P., Hanchar, J.M. (2000): Radioluminescence and thermoluminescence of rare earth elements and phosphorus-doped zircon. *Am. Mineral.*, **85**, 668–681.
- Kempe, U., Gruner, T., Renno, A.D., Wolf, D. (1997): Hf-rich zircons in rare-metal bearing granites: Magmatic or metasomatic origin? in “Mineral deposits: Research and exploration. Where do they meet?”, H. Papunen, ed. Balkema, Rotterdam, 643–646.
- Kempe, U., Gruner, T., Nasdala, L., Wolf, D. (2000): Relevance of cathodoluminescence for interpretation of U-Pb zircon ages (with an example of application to a study of zircons from the Saxonian Granulite Complex, Germany). in “Cathodoluminescence in Geosciences”, M. Pagel, V. Barbin, P. Blanc, D. Ohnenstetter, ed. Springer, Berlin, 415–455.
- Kempe, U., Bombach, K., Matukov, D., Schlothauer, T., Hutschenreuter, J., Wolf, D., Sergeev, S. (2004): Pb/Pb and U/Pb zircon dating of subvolcanic rhyolite as a time marker for Hercynian granite magmatism and Sn mineralisation in the Eibenstock granite, Erzgebirge, Germany: Considering effects of zircon alteration. *Mineral. Dep.*, **39**, 646–669.
- Kempe, U., Seltmann, R., Graupner, T., Rodionov, N., Sergeev, S. A., Matukov, D.I., Kremenetsky A.A. (2015): Concordant U-Pb SHRIMP ages of U-rich zircon in granitoids from the Muruntau gold district (Uzbekistan): Timing of intrusion, alteration ages, or meaningless numbers. *Ore Geol. Rev.*, **65**, 308–326.
- Kempe, U., Thomas, S.M., Geipel, G., Thomas, R., Plötze, M., Böttcher, R., Grambole, G., Hoentsch, J., Trinkler, M. (2010): Optical absorption, luminescence, and electron paramagnetic resonance (EPR) spectroscopy of crystalline to metamict zircon: Evidence for formation of uranyl, manganese, and other optically active centers. *Am. Mineral.*, **95**, 335–347.
- Kempe, U., Trinkler, M., Pöppel, A., Himcinschi, C. (2016): Coloration of natural zircon. *Can. Mineral.*, **54**, 635–660.
- Knittel, E. & Williams, Q. (1993): High-pressure Raman spectroscopy of  $ZrSiO_4$ : Observation of the zircon to scheelite transition at 300 K. *Am. Mineral.*, **78**, 245–252.
- Kranert, C., Sturm, C., Schmidt-Grund, R., Grundmann, M. (2016): Raman tensor formalism for optically anisotropic crystals. *Phys. Rev. Lett.*, **116**, 1–5.
- Lenz, C. & Nasdala, L. (2015): A photoluminescence study of  $REE^{3+}$  emissions in radiation-damaged zircon. *Am. Mineral.*, **100**, 1123–1133.
- Lenz, C., Talla, D., Ruschel, K., Skoda, R., Götze, J., Nasdala, L. (2013): Factors affecting the  $Nd^{3+}$  ( $REE^{3+}$ ) luminescence of minerals. *Mineral. Petrol.*, **107**, 415–428.
- Ludwig, K.R. (2000): SQUID 1.00: A User’s Manual. Berkeley Geochronology Center Special Publication No 2, 2455 Ridge Road, Berkeley CA 94709, USA.
- Marsellos, A.E. & Garvers, J.I. (2010): Radiation damage and uranium concentration in zircon as assessed by Raman spectroscopy and neutron irradiation. *Am. Mineral.*, **95**, 1192–1201.
- Meldrum, A., Boatner, L.A., Zinkle, S.J., Wang, S.X., Wang, L.M., Ewing, R.C. (1999): Effects of dose rate and temperature on the crystalline-to-metamict transformation in the  $ABO_4$  orthosilicates. *Can. Mineral.*, **37**, 207–221.

- Murakami, T., Chakoumakos, B.C., Ewing, R.C., Lumpkin, G.R., Weber, W.J. (1991): Alpha-decay event damage in zircon. *Am. Mineral.*, **76**, 1510–1532.
- Nasdala, L., Irmer, G., Wolf, D. (1995): The degree of metamictization in zircon: A Raman spectroscopic study. *Eur. J. Mineral.*, **7**, 471–478.
- Nasdala, L., Pidgeon, R.T., Wolf, D., Irmer, G. (1998): Metamictization and U–Pb isotopic discordance in single zircons: a combined Raman microprobe and SHRIMP ion probe study. *Mineral. Petrol.*, **62**, 1–27.
- Nasdala, L., Wenzel, M., Vavra, G., Irmer, G., Wenzel, T., Kober, B. (2001): Metamictization of natural zircon: accumulation vs. thermal annealing of radioactivity-induced damage. *Contrib. Mineral. Petrol.*, **141**, 125–144.
- Nasdala, L., Irmer, G., Jonckheere, R. (2002a): Radiation damage ages: Practical concept or impractical vision? – Reply to two comments on “Metamictization of natural zircon: Accumulation versus thermal annealing of radioactivity-induced damage”, and further discussion. *Contrib. Mineral. Petrol.*, **143**, 758–765.
- Nasdala, L., Lengauer, C.L., Hanchar, J.M., Kronz, A., Wirth, R., Blanc, P., Kennedy, A.K., Seydoux-Guillaume, A.-M. (2002b): Annealing radiation damage and the recovery of cathodoluminescence. *Chem. Geol.*, **191**, 121–140.
- Nasdala, L., Zhang, M., Kempe, U., Panczer, G., Gaft, M., Andrut, M., Plötze, M. (2003): Spectroscopic methods applied to zircon. in “Zircon”, J.M. Hanchar, P.W.O. Hoskin, ed. Reviews in Mineralogy and Geochemistry, 53, Mineralogical Society of America, Washington D.C., 145–181.
- Nasdala, L., Rainers, P.W., Garver, J.I., Kennedy, A.K., Stern, R.A., Balan, E., Wirth, R. (2004): Incomplete retention of radiation damage in zircon from Sri Lanka. *Am. Mineral.*, **89**, 219–231.
- Nasdala, L., Hanchar, J.M., Kronz, A., Whitehouse, M.J. (2005): Long-term stability of alpha particle damage in natural zircon. *Chem. Geol.*, **220**, 83–103.
- Nasdala, L., Kronz, A., Hanchar, J.M., Tichomirowa, M., Davis, D. W., Hofmeister, W. (2006): Effects of natural radiation damage on back-scattered electron images of single crystals of minerals. *Am. Mineral.*, **91**, 1739–1746.
- Nasdala, L., Miletich, R., Ruschel, K., Váczi, T. (2008): Raman study of radiation-damaged zircon under hydrostatic compression. *Phys. Chem. Mineral.*, **35**, 597–602.
- Nasdala, L., Kronz, A., Wirth, R., Váczi, T., Pérez-Soba, C., Willner, A., Kennedy, A.K. (2009): The phenomenon of deficient electron microprobe totals in radiation-damaged and altered zircon. *Geochim. Cosmochim. Acta*, **73**, 1637–1650.
- Nasdala, L., Hanchar, J.M., Rhede, D., Kennedy, A.K., Váczi, T. (2010): Retention of uranium in complexly altered zircon: An example from Bancroft, Ontario. *Chem. Geol.*, **269**, 290–300.
- Nelson, D.R., Robinson, B.W., Myers, J.S. (2000): Complex geological histories extending for  $\geq 4.0$  Ga deciphered from xenocryst zircon microstructures. *Earth Planet. Sci. Lett.*, **181**, 89–102.
- Oliver, W.C., McCallum, J.C., Chakoumakos, B.C., Boatner, L.A. (1994): Hardness and elastic modulus of zircon as a function of heavy-particle irradiation dose: II. Pb-ion implantation damage. *Rad. Eff. Def. Solid.*, **132**, 131–141.
- Özkan H. (1976): Effect of nuclear radiation on the elastic moduli of zircon. *J. Appl. Phys.*, **47**, 4772–4779.
- Özkan, H & Jamieson, J.C. (1978): Pressure dependence of the elastic constants of nonmetamict zircon. *Phys. Chem. Minerals*, **2**, 215–224.
- Palenik, Ch.S., Nasdala, L., Ewing R.C. (2003): Radiation damage in zircon. *Am. Mineral.*, **88**, 770–781.
- Park, B., Weber, W.J., Corrales, L.R. (2001): Molecular-dynamics simulation study of threshold displacements and defect formation in zircon. *Phys. Rev. B*, **64**, 174108-1–174109-16.
- Pérez-Soba, C., Villaseca, C., González del Tánago, J., Nasdala, L. (2007): The composition of zircon in the peraluminous Hercynian granites of the Spanish Central System batholith. *Can. Mineral.*, **45**, 509–527.
- Platt, R.G. & Woolley, A.R. (1986): The mafic mineralogy of the peralkaline syenites and granites of the Mulanje complex, Malawi. *Mineral. Mag.*, **50**, 85–99.
- Platt, R.G., Wall, F., Williams, C.T., Woolley, A.R. (1987): Zirconolite, chevkinite and other rare earth minerals from nepheline syenites and peralkaline granites and syenites of the Chilwa Alkaline Province, Malawi. *Mineral. Mag.*, **51**, 253–263.
- Pointer, C.M., Ashworth, J.R., Ixer, R.A. (1988): The zircon-thorite mineral group in metasomatized granite, Ririwai, Nigeria. 2. Zoning, alteration and exsolution in zircon. *Mineral. Petrol.*, **39**, 21–37.
- Presser, V. & Glotzbach, C. (2009): Metamictization in zircon: Raman investigation following a Rietveld approach. Part II: Sampling depth implication and experimental data. *J. Raman Spectr.*, **40**, 499–508.
- Puppels, G.J., Colier, W., Olminkhof, J.H.F., Otto, C., de Mul, F.F., Greve, J. (1991): Description and performance of a highly sensitive confocal Raman microspectrometer. *J. Raman Spectr.*, **22**, 217–223.
- Pyatenko, Y.A. (1970): On the behaviour of metamict minerals during heating under respect of the general problem of metamictization. *Geokhimiya*, **9**, 1077–1083.
- Reddy, S.M., Timms, N.E., Trimby, P., Kinny, P.D., Buchan, C., Blake, K. (2006): Crystal-plastic deformation of zircon: A defect in the assumption of chemical robustness. *Geology*, **34**, 257–260.
- Reddy, S.M., Timms, N.E., Hamilton, P.J., Smyth, H.R. (2009): Deformation of microstructure in magmatic zircon and implications for diffusion. *Contrib. Mineral. Petrol.*, **157**, 231–244.
- Ríos, S. & Salje, E.K.H. (1999): Diffuse x-ray scattering from weakly metamict zircon. *J. Phys. Condens. Matt.*, **11**, 8947–8956.
- Ríos, S., Malcherek, T., Salje, E.K.H., Domeneghetti, C. (2000a): Localized defects in radiation-damaged zircon. *Acta Crystallogr. B*, **56**, 947–952.
- Ríos, S., Salje, E.K.H., Zhang, M., Ewing, R.C. (2000b): Amorphization in zircon: evidence for direct impact damage. *J. Phys.: Condens. Matt.*, **12**, 2401–2412.
- Rizzo, G., Spiess, R., Hanchar, J.M. (2000): Non xenotime-type substitution within zircon: implications for lattice distortion. in “Integrative geosciences solutions: A start for the new millennium”, American Geophysical Union 2000 Spring Meeting, Washington D.C. Program with Abstracts, GS31A-05.
- Rudenko, S.A. (1968): The phenomenon of metamict decay of minerals and its position in mineral formation processes. *Zap. Vses. Mineral. Obshch.*, **97**, 565–570 (in Russian).

- Sahama, T.G. (1981): Growth structure in Ceylon zircon. *Bull. Minéral.*, **104**, 89–94.
- Salje, E.K.H., Chrosch, J., Ewing, R.C. (1999): Is “metamictization” of zircon a phase transition? *Am. Mineral.*, **84**, 1107–1116.
- Sanjurjo, J.A., Lopez-Cruz, E., Burns, G. (1983): High-pressure Raman study of zone centre phonons in PbTiO<sub>3</sub>. *Phys. Rev. B*, **28**, 7260–7268.
- Smith, D.G.W., de St. Jorre, L., Reed, S.J.B., Long, J.V.P. (1991): Zonally metamictized and other zircons from Thor Lake, Northwest Territories. *Can. Mineral.*, **29**, 301–309.
- Soltsev, V.P. & Shcherbakova, M.Y. (1972): Electron spin resonance of Ti<sup>3+</sup> in α-quartz and zircon. *J. Struct. Chem.*, **13**, 859–861.
- , — (1974): Mechanism of charge compensation and substitution of Nb and Y in the zircon structure. *Neorg. Mater.*, **10**, 1834–1838 (in Russian).
- Soman, A., Geisler, T., Tomaschek, F., Grange, M., Berndt, J. (2010): Alteration of crystalline zircon solid solutions: a case study on zircon from an alkaline pegmatite from Zomba-Malosa, Malawi. *Contrib. Mineral. Petrol.*, **160**, 909–930.
- Speer, J.A. (1982): Zircon. in “Orthosilicates”, P.H. Ribbe, ed. Reviews in Mineralogy, 5, Mineralogical Society of America, Washington D.C., second edition, 67–112.
- Speer, J.A. & Cooper, B.J. (1982): Crystal structure of synthetic hafnon, HfSiO<sub>4</sub>, comparison with zircon and the actinide orthosilicates. *Am. Mineral.*, **67**, 804–808.
- Syme, R.W.G., Lockwood, D.J., Kerr, H.J. (1977): Raman spectrum of synthetic zircon (ZrSiO<sub>4</sub>) and thorite (ThSiO<sub>4</sub>). *J. Phys. C: Solid State Phys.*, **10**, 1335–1348.
- Tichomirowa, M., Whitehouse, M.J., Nasdala, L. (2005): Resorption, growth, solid state recrystallisation, and annealing of granulite facies zircon – a case study from the Central Erzgebirge, Bohemian Massif. *Lithos*, **82**, 25–50.
- Trofimov, A.K. (1962): The nature of the line luminescence spectra of zircon. *Geokhimiya*, **11**, 970–975 (in Russian).
- Ushikubo, T., Kita, N.T., Cavosie, A.J., Wilde, S.A., Rudnick, R.L., Valley, J.W. (2008): Lithium in Jack Hills zircons: Evidence for extensive weathering of Earth’s earliest crust. *Earth Planet. Sci. Lett.*, **272**, 666–676.
- Vance, E.R. & Mackey, D.J. (1974): Optical study of U<sup>5+</sup> in zircon. *J. Phys. C: Solid State Phys.*, **7**, 1898–1908.
- , — (1978): Optical spectra of U<sup>4+</sup> and U<sup>5+</sup> in zircon, hafnon, and thorite. *Phys. Rev. B*, **18**, 185–189.
- Vinokurov, V.M., Zaripov, M.M., Stepanov, V.G., Chirkin, G.K., Shekun, L.Y. (1964): Paramagnetic resonance of Nb<sup>4+</sup> ions in zircon single crystals. *Sov. Phys. Solid State*, **5**, 1487–1488.
- Votyakov, S.L. & Samojlov, M.V. (1981): Defects in zircon and its thermoluminescence. in “Crystallochemical peculiarities of silicate minerals from the Urals”, Ural Scientific Centre of the Academy of Sciences of the SSSR, 45–52 (in Russian).
- Votyakov, S.L., Krokhaliev, V.Y., Krasnobaev, A.A. (1985): Recombination luminescence in zircon. *Zhur. Priklad. Spekt.*, **42**, 928–935 (in Russian).
- Wang, X.L., Coble, M.A., Valley, J.W., Shu, X.J., Kitajima, K., Spicuzza, M.J., Sun, T. (2014): Influence of radiation damage on Late Jurassic zircon from southern China: Evidence from *in situ* measurements of oxygen isotopes, laser Raman, U–Pb ages, and trace elements. *Chem. Geol.* **389**, 122–136.
- Wang, W., Scarratt, K., Emmett, J.L., Breeding, C.M., Douthit, T.R. (2006): The effects of heat treatment on zircon inclusions in Madagascar sapphires. *Gems & Gemology*, **42**, 134–150.
- Wasilewski, P.J., Senftle, F.E., Vaz, J.A., Thorpe, A.N., Alexander, C.C. (1973): A study of the natural α-recoil damage in zircon by infrared spectra. *Rad. Eff.*, **17**, 191–199.
- Weber, W.J. & Maupin, G.D. (1988): Simulation of radiation damage in zircon. *Nucl. Instr. Meth. Phys. Res.*, **B32**, 512–515.
- Wiedenbeck, M., Alle, P., Corfu, F., Griffin, W.L., Meier, M., Oberli, F., von Quadt, A., Roddick, J.C., Spiegel, W. (1995): Three natural zircon standards for U–Th–Pb, Lu–Hf, trace element and REE analysis. *Geostand. Newslett.*, **19**, 1–3.
- Williams, I.S. (1998): U–Th–Pb geochronology by ion microprobe. in “Applications of Microanalytical Techniques to Understanding Mineralizing Processes”, M.A. McKibben, I.W.C. Shanks, W.J. Ridley, ed. Reviews in Economic Geology, 1–35.
- Woodhead, J.A., Rossman, G.R., Silver, L.T. (1991): The metamictization of zircon: Radiation dose-dependent structural characteristics. *Am. Mineral.*, **76**, 74–82.
- Woolley, A.R. (1987): Lithosphere metasomatism and the petrogenesis of the Chilwa Province of alkaline igneous rocks and carbonatites, Malawi. *J. Afr. Earth Sci.*, **6**, 891–898.
- Woolley, A.R. & Jones, G.C. (1987): The petrochemistry of the northern part of the Chilwa alkaline province, Malawi. in “Alkaline igneous rocks”, J.G. Fitton, B.G.J. Upton, ed. Geological Society Special Publication, London, **30**, 335–355.
- Woolley, A.R. & Platt, R.G. (1986): The mineralogy of nepheline syenite complexes from the northern part of the Chilwa Province, Malawi. *Mineral. Mag.*, **50**, 597–610.
- Zhang, M. & Salje, E.K.H. (2001): Infrared spectroscopic analysis of zircon: Radiation damage and the metamict state. *J. Phys.: Condens. Matt.*, **13**, 3057–3071.
- Zhang, M., Salje, E.K.H., Farnan, I., Graeme-Barber, A., Daniel, P., Ewing, R.C., Clark, A.M., Leroux, H. (2000): Metamictization of zircon: Raman spectroscopic study. *J. Phys.: Condens. Matt.*, **12**, 1915–1925.
- Zhang, M., Salje, E.K.H., Ewing, R.C. (2003): Oxidation state of uranium in metamict and annealed zircon: near-infrared spectroscopic quantitative results. *J. Phys.: Condens. Matt.*, **15**, 3445–3470.
- Zhirov, K.K. (1952): On the transition of zircon into the metamict state. *Dokl. Akad. Nauk SSSR*, **85**, 889–891 (in Russian).

Received 13 April 2017

Modified version received 26 September 2017

Accepted 30 January 2018